

Probing anomalous $W^-W^+\gamma/Z$ couplings in the SMEFT with $e^-e^+ \rightarrow W^-W^+ \rightarrow 4j/\ell^-\ell^+\not{E}$ channel

Amir Subba ^{a,b}, Ritesh K. Singh ^a

^aDepartment of Physical Sciences, Indian Institute of Science Education and Research Kolkata, Mohanpur, 741246, India

^bDepartment of Physics, Indian Institute of Technology Guwahati, Guwahati, Assam, 781039, India

E-mail: amirsubba@iitg.ac.in, ritesh.singh@iiserkol.ac.in

ABSTRACT: We investigate anomalous charged triple gauge boson couplings induced by $SU(2)_L \times U(1)_Y$ gauge-invariant dimension-6 operators in the HISZ basis via the processes $e^-e^+ \rightarrow 4j$ and $e^-e^+ \rightarrow \ell^-\ell^+\not{E}$ at $\sqrt{s} = 250$ GeV with longitudinally polarized beams. The analysis includes three CP-even operators, $(\mathcal{O}_{WWW}, \mathcal{O}_W, \mathcal{O}_B)$, and two CP-odd operators, $(\mathcal{O}_{\widetilde{W}WW}, \mathcal{O}_{\widetilde{W}})$, which parameterize deviations in the $W^-W^+\gamma/Z$ vertex. All leading-order contributions are taken into account, including the interference of W^-W^+ production with non-resonant amplitudes. In the case of $e^-e^+ \rightarrow 4j$ events, W^-W^+ candidates are selected using boosted decision trees (BDT). The W -boson charges are reconstructed from jet-charge observable, and the jet flavors from W decays are identified with a dedicated BDT, enabling the extraction of vector polarization and associated correlation asymmetries. In the $e^-e^+ \rightarrow \ell^-\ell^+\not{E}$ channel, W^-W^+ events are selected with kinematic cuts on p_T^ℓ and $m_{\ell^-\ell^+}$, and the two neutrino momenta are reconstructed using neural-network regression. The combination of the total cross section and spin asymmetries is used to constrain anomalous gauge couplings. We find that the fully hadronic channel yields the strongest sensitivity to \mathcal{O}_B and $\mathcal{O}_{\widetilde{W}}$, while the semi-leptonic channel provides tighter constraints on \mathcal{O}_{WWW} , \mathcal{O}_W and $\mathcal{O}_{\widetilde{W}WW}$. The fully leptonic channel adds complementary sensitivity. Finally, we derive marginalized limits on all five operators using a Markov Chain Monte Carlo analysis for several choices of systematic uncertainties and integrated luminosities.

Contents

1	Introduction	1
2	Polarization and spin correlations	6
3	Collider analysis of $e^-e^+ \rightarrow 4j$ events	9
3.1	Event selection with boosted decision trees	10
3.2	Reconstruction of oppositely charged two W bosons	12
3.3	Decision trees based flavor tagging of W^\pm jets	14
4	Collider analysis of $e^-e^+ \rightarrow \ell^-\ell^+\not{E}$ events	17
4.1	Reconstruction of two missing neutrinos	19
5	SMEFT analysis	20
5.1	MCMC analysis with combined channels	28
6	Conclusion	30

1 Introduction

The discovery of weak intermediate vector bosons, W^\pm by the UA1 [1] and UA2 [2] collaboration and Z boson [3, 4] by the same collaboration at CERN supports the $SU(2)_L \times U(1)_Y$ gauge structure of the Standard Model (SM) of particle physics. The final validation of the SM was done with the discovery of Higgs boson by CMS and ATLAS collaboration at LHC. Nevertheless, there exist a loophole within the SM that questions the completeness of the SM. The stability of the Higgs mass under radiative corrections, neutrino oscillation and mass, dark matter are some of boiling questions which SM fails to answer. After the discovery of Higgs boson, the precision measurement of the parameters in the Higgs sector could potentially signal the presence of new physics if there is any. Also, directly related to the Higgs sector is the implications of electroweak gauge structure of the SM viz., triple gauge boson couplings (TGC) and quartic gauge couplings (QGC) among the charged and neutral bosons. Thus, measurement of TGC and QGC could directly shed light on gauge structure and the electroweak symmetry breaking (EWSB) of the SM.

Experiments at LHC like CMS [5–8] and ATLAS [9–14] had extensively studied TGC, viz., $W^-W^+V, V \in \{\gamma, Z\}$ couplings in various di-boson process with semi-leptonic and full-leptonic final decayed states. On the theoretical side, various studies are available that employed different techniques to probe anomalous TGC (aTGC). For instance, Refs. [15, 16] utilize the polarizations of W boson to constrain aTGC and in study [17–19], additional spin correlations parameters of WW di-boson are incorporated to effectively constrain aTGC. Optimal observable technique (OOT) based limits on aTGC are provided in Ref. [20, 21].

Modern machine learning (ML) based techniques has also been used in order to probe aTGC in di-boson process [18, 22]. The quantum tomography [23, 24] based study of anomalous $W^-W^+\gamma/Z$ has also been done.

The search for the deviation in the W^-W^+V are usually performed in two different framework. One follows the construction of most general Lagrangian involving two charge boson and one neutral boson from which required vertex term are read out. This approach is usually known as LEP framework developed in 1980 assuming $U(1)_{\text{EM}}$ and Lorentz invariance, and the Lagrangian is given in terms of 14 anomalous parameters as [25]

$$\begin{aligned} \mathcal{L}_{WWV} = & ig_{WWV} \left[g_1^V (W_{\mu\nu}^+ W^{-\mu} - W^{+\mu} W_{\mu\nu}^-) V^\nu + k_V W_\mu^+ W_\nu^- V^{\mu\nu} + \frac{\lambda_V}{m_W^2} W_\mu^{\nu+} W_\nu^{-\rho} V_\rho^\mu \right. \\ & + ig_4^V W_\mu^+ W_\nu^- (\partial^\mu V^\nu + \partial^\nu V^\mu) - ig_5^V \epsilon^{\mu\nu\rho\sigma} (W_\mu^+ \partial_\rho W_\nu^- - \partial_\rho W_\mu^+ W_\nu^-) V_\sigma \\ & \left. + \tilde{k}_V W_\mu^+ W_\nu^- \tilde{V}^{\mu\nu} + \frac{\tilde{\lambda}_V}{m_W^2} W_\mu^{\nu+} W_\nu^{-\rho} \tilde{V}_\rho^\mu \right], \end{aligned} \quad (1.1)$$

where $W_{\mu\nu}^\pm = \partial_\mu W_\nu^\pm - \partial_\nu W_\mu^\pm$, $V_{\mu\nu} = \partial_\mu V_\nu - \partial_\nu V_\mu$, $g_{WW\gamma} = -e$ and $g_{WWZ} = -e \cot \theta_W$, where e and θ_W are the proton charge and weak mixing angle respectively. The dual field is defined as $\tilde{V}^{\mu\nu} = 1/2 \epsilon^{\mu\nu\rho\sigma} V_{\rho\sigma}$, with Levi-Civita tensor $\epsilon^{\mu\nu\rho\sigma}$ follows a standard convention, $\epsilon^{0123} = 1$. Within the SM, the value of the couplings are $g_1^Z = g_1^\gamma = k_Z = k_\gamma = 1$ and all others are zero. The couplings g_1^V, k_V , and λ_V are CP-even, while g_4^V is odd in C and P-even, \tilde{k}_V and $\tilde{\lambda}_V$ are C-even and P-odd and the last coupling g_5^V is C and P-odd which make it CP-even. The search for anomalous signature based on parameterization of Eq. (1.1) has some subtle issues as was pointed out in Ref. [26]; the theory can be expanded to infinitum by adding derivative normalized by mass of W bosons and those terms are not suppressed at energies above W mass, unless the anomalous couplings are very small. On the absence of concrete evidence for new particles at the LHC, one is generally lead to assume that, new physics (NP) if any, must be too heavy to be observed in the current energy scale. However, even if the NP is too heavy, one can work with the residual effect of such heavy physics at the electroweak scale through some parameters, usually known as Wilson's coefficient (WC). These WCs are associated with higher dimensional ($d > 4$) operators constructed out of the SM states. The SM effective field theory (SMEFT) provides a systematic and model-independent framework to parameterize the low-energy effects of heavy new physics beyond the SM in terms of higher-dimensional, $SU(3)_C \times SU(2)_L \times U(1)_Y$ gauge-invariant operators constructed solely from SM fields [27, 28]. In this framework, the effective Lagrangian is expressed as an expansion in powers of the cutoff scale Λ , which denotes the characteristic energy scale of new physics [27],

$$\mathcal{L}_{\text{EFT}} = \mathcal{L}_{\text{SM}} + \frac{1}{\Lambda} \sum_i c_i^{(5)} \mathcal{O}_i^{(5)} + \frac{1}{\Lambda^2} \sum_i c_i^{(6)} \mathcal{O}_i^{(6)} + \dots, \quad (1.2)$$

where $\mathcal{O}_i^{(d)}$ are the dimension- d operators constructed from SM fields, and $c_i^{(d)}$ are the corresponding WCs encoding the effects of the ultraviolet (UV) theory. Assuming baryon and lepton number conservation, the lowest-order nontrivial corrections to the SM arise from dimension-6 operators, as dimension-5 terms induce Majorana neutrino masses and

violate lepton number [29]. Given that Λ is typically expected to lie in the TeV range, higher-order contributions ($d > 6$) can be safely neglected, and the EFT expansion can be truncated at $\mathcal{O}(1/\Lambda^2)$.

In this work, we restrict ourselves to the subset of dimension-6 operators relevant for anomalous triple gauge-boson interactions, following the Hagiwara–Ishihara–Szalapski–Zeppenfeld (HISZ) basis [30]. The effective Lagrangian in this basis can be written as

$$\begin{aligned} \mathcal{L}_{WWV}^{(6)} = & \frac{c_{WWV}}{\Lambda^2} \text{Tr}[W_{\nu\rho} W^{\mu\nu} W_{\mu}^{\rho}] + \frac{c_W}{\Lambda^2} (D_{\mu}\Phi)^{\dagger} W^{\mu\nu} (D_{\nu}\Phi) + \frac{c_B}{\Lambda^2} (D_{\mu}\Phi)^{\dagger} B^{\mu\nu} (D_{\nu}\Phi) \\ & + \frac{c_{\widetilde{W}WW}}{\Lambda^2} \text{Tr}[\widetilde{W}_{\mu\nu} W^{\nu\rho} W_{\rho}^{\mu}] + \frac{c_{\widetilde{W}}}{\Lambda^2} (D_{\mu}\Phi)^{\dagger} \widetilde{W}^{\mu\nu} (D_{\nu}\Phi), \end{aligned} \quad (1.3)$$

where Φ is the Higgs doublet, and the covariant derivative and field-strength tensors are defined as

$$\begin{aligned} D_{\mu} &= \partial_{\mu} + \frac{i}{2} g \tau^i W_{\mu}^i + \frac{i}{2} g' B_{\mu}, \\ W_{\mu\nu} &= \frac{i}{2} g \tau^i (\partial_{\mu} W_{\nu}^i - \partial_{\nu} W_{\mu}^i + g \epsilon_{ijk} W_{\mu}^j W_{\nu}^k), \\ B_{\mu\nu} &= \frac{i}{2} g' (\partial_{\mu} B_{\nu} - \partial_{\nu} B_{\mu}). \end{aligned} \quad (1.4)$$

Here, g and g' denote the $SU(2)_L$ and $U(1)_Y$ gauge couplings, respectively. Among the operators in Eq. (1.3), the first three are CP-even, while the last two are CP-odd. These operators encapsulate the leading-order deviations from the SM gauge-boson self-interactions in a model-independent manner. On matching the WCs with the anomalous parameters in Eq. (1.1), one obtain the following relation between the two theory as

$$\begin{aligned} \Delta g_1^Z &= \frac{c_W m_Z^2}{2\Lambda^2}, \quad \Delta \kappa_{\gamma} = \frac{(c_W + c_B) m_W^2}{2\Lambda^2}, \quad \Delta \kappa_Z = \frac{(c_W - c_B \tan^2_W) m_W^2}{2\Lambda^2}, \\ \lambda_{\gamma} = \lambda_Z &= \frac{c_{WWV} 3g^2 m_W^2}{2\Lambda^2}, \quad g_4^V = g_5^V = 0, \quad \tilde{\kappa}_{\gamma} = \frac{c_{\widetilde{W}} m_W^2}{2\Lambda^2}, \\ \tilde{\kappa}_Z &= -\frac{c_{\widetilde{W}} \tan^2 \theta_W m_W^2}{2\Lambda^2}, \quad \tilde{\lambda}_{\gamma} = \tilde{\lambda}_Z = \frac{c_{\widetilde{W}WW} 3g^2 m_W^2}{2\Lambda^2}. \end{aligned} \quad (1.5)$$

The presence of anomalous couplings at the vertex would modify both the angular and kinematic distributions of final decayed particles from the SM values. The effects of anomalous $W^-W^+\gamma/Z$ couplings on various kinematic and spin-related observables have been theoretically studied in several works [15–18, 31–36].

Most experimental searches for deviations from the SM in W^-W^+ production have concentrated on the semi-leptonic channel, which delivers a favorable compromise between reconstruction fidelity and event yield. Nevertheless, the dominant hadronic branching fraction of the W^{\pm} boson implies that the fully hadronic final state contains a large statistical sample and therefore constitutes a valuable, and in many respects complementary, probe of physics beyond the SM. In this work we perform a comparative study of the $e^-e^+ \rightarrow W^-W^+$ process in both the fully hadronic ($4j$) and fully leptonic ($\ell^+\ell^-\not{E}$) final states at a polarized e^-e^+ collider, with the aim of constraining anomalous $W^-W^+\gamma$ and W^-W^+Z couplings in a model-independent SMEFT framework.

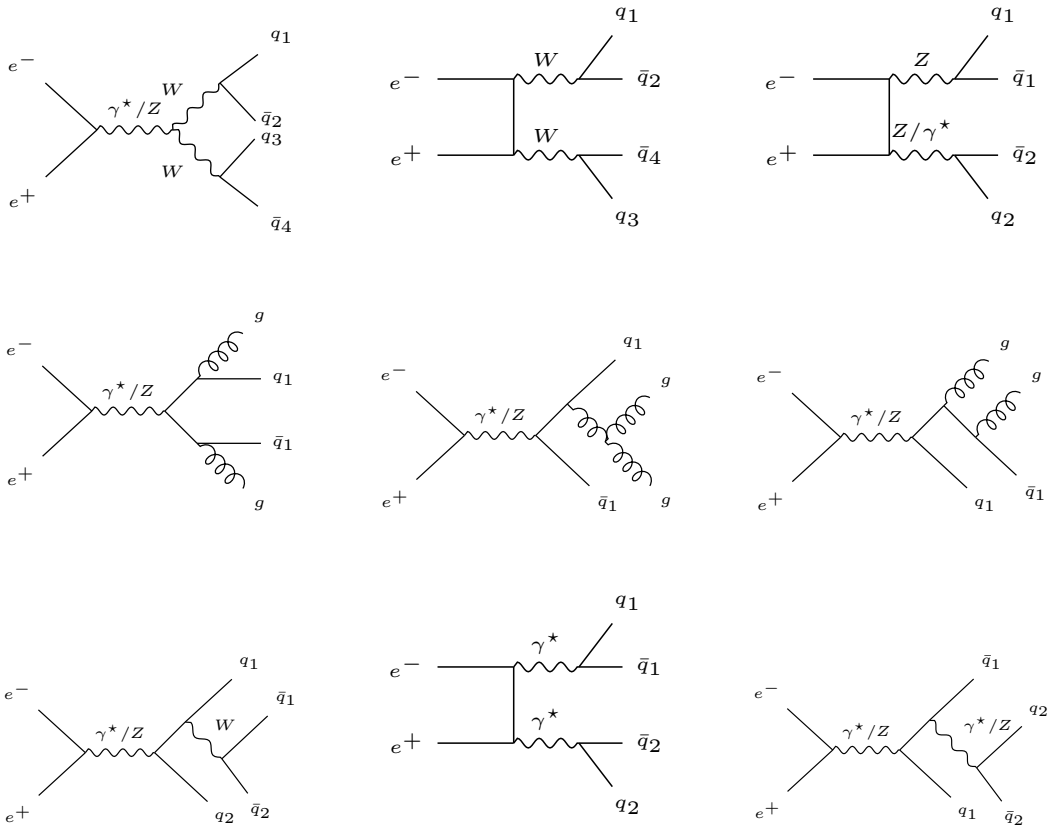


Figure 1: Schematic Feynman diagrams at lowest order for $4j$ events in final state at e^-e^+ collider. The top row represents the one/two-resonant ZZ/γ , and W^-W^+ amplitudes with coupling order of α_{EW}^2 . The middle row amplitudes represents gluons in the final state of order $\alpha_{EW}\alpha_S$, and the bottom row contains zero-resonant amplitudes with four quarks in final states with coupling order of α_{EW}^2 .

For the four-jet final state the on-shell W^-W^+ contribution is embedded within a larger, gauge-invariant set of Feynman amplitudes. At leading electroweak order the irreducible backgrounds comprise ZZ , $Z\gamma^*$ and other non-resonant continuum topologies contributing at $\mathcal{O}(\alpha_{EW}^2)$. In addition, reducible QCD-induced topologies with final-state gluons enter at mixed orders such as $\mathcal{O}(\alpha_{EW}\alpha_S)$ and higher, and must be included for a realistic estimate of the $4j$ final-state rate. Representative LO diagrams for the four-jet topology are shown in Fig. 1. In the current article, we have considered all possible LO $4j$ amplitudes.

By contrast, the fully leptonic channel, $e^-e^+ \rightarrow \ell^-\ell^+\cancel{E}$, has the smallest branching fraction but offers a remarkably clean experimental environment. The schematic LO amplitudes for the dileptonic topology are shown in Fig. 2. Two well-reconstructed charged leptons and large missing transverse energy provide powerful kinematic handles and strong background suppression. The reconstruction of W -boson kinematics, however, is affected

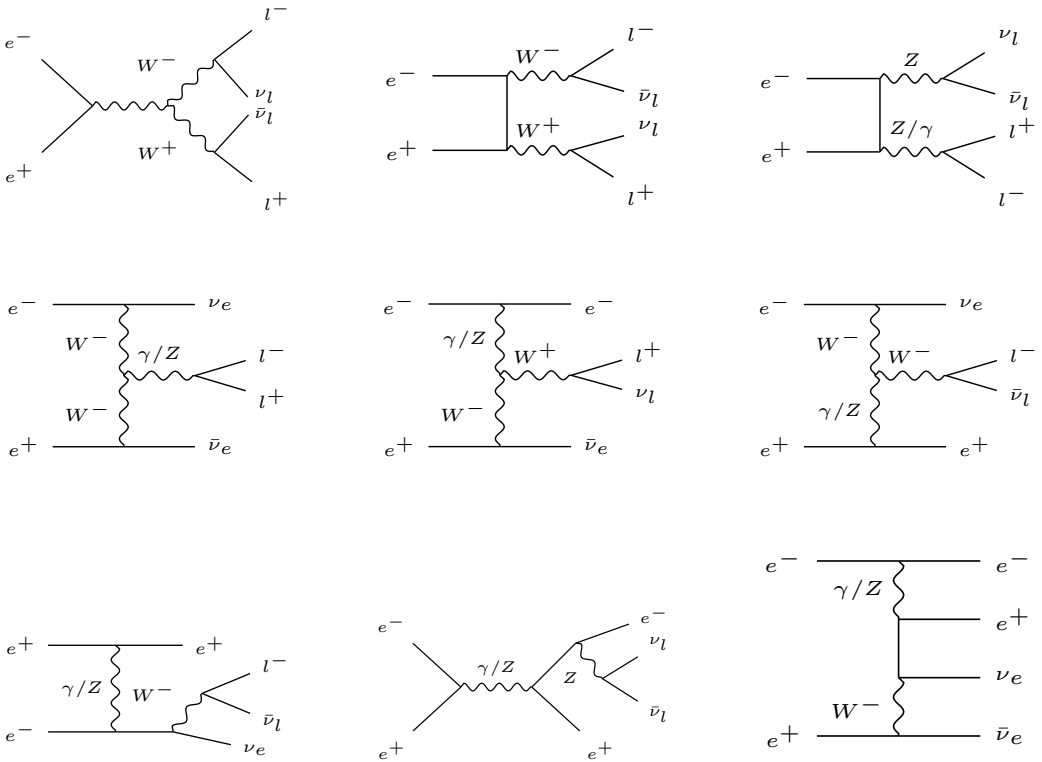


Figure 2: Schematic representation of Feynman diagrams for $e^-e^+ \rightarrow l^-l^+\not{E}$ process at the leading order.

by neutrino-related ambiguities, while in the hadronic case, showering and hadronization complicate the interpretation of WW kinematics. Nevertheless, interference between resonant and non-resonant diagrams can enhance sensitivity beyond the statistical advantage of the hadronic mode and partly compensate for the low rate of the leptonic one. Due to differences in the final states (and hence interferences) they show different sensitivity to anomalous couplings. Consequently, they yield complementary constraints as will be discussed latter.

The remainder of this article is organized as follows. Section 2 introduces the formalism for describing the W^+W^- polarization states and spin correlations, and outlines the extraction of these observables from joint angular distributions of the final-state jets. Section 3 details the collider simulation and event-selection strategy, including signal–background separation using a Boosted Decision Tree (BDT). After selecting W^-W^+ -like signal events, jet-charge based tagging is applied to assign W^- and W^+ candidates. A jet-level flavor-tagging BDT is then used to classify the decay jets of each W boson into *up-* or *down-type* categories, as described in Section 3.3. In Section 4, we discuss the collider analysis of full-leptonic channel along with the reconstruction of two missing neutrinos using artificial neural network. The analysis and results on anomalous $W^-W^+\gamma$ and W^-W^+Z couplings within the SMEFT framework are presented in Section 5, followed by

conclusions in Section 6.

2 Polarization and spin correlations

The spin of a particle is a fundamental property that influences the Lorentz structure of its interactions with other SM particles, and understanding these interactions is essential for probing SM or any beyond SM theories [37–39]. On the other hand, the spin of a particle also dictates the angular distribution of decayed particles, which can be influenced by the change in the interaction. Thus, the change in couplings due to the presence of new physics may lead to deviation of various angular functions of final state particles from the SM value. Based on the value of spin of a decaying particle, we can quantify these angular functions in terms of polarization parameters. In particular, for a spin-1 particle like W boson, 8 independent polarization parameters holds the information of production dynamics which can be obtained by using the angular distribution of the decayed daughter. And in a process where two spin-1 boson (W^-W^+) are produced, the production dynamics are encoded in 16 polarizations, and 64 spin correlations, which can be obtained in terms of the polar and azimuth angle of final decayed fermions. We list the correlators f'_i 's in terms of angular functions of final decayed fermions, and the related generators in Table 1.

Table 1: List of angular functions that are associated with the distribution of final decayed fermions and the corresponding generators.

Correlators	Functions	Generators
f_0	1	$J_0 = \mathbb{I}$
f_1	$\sin \theta \cos \phi$	$J_1 = S_x/2$
f_2	$\sin \theta \sin \phi$	$J_2 = S_y/2$
f_3	$\cos \theta$	$J_3 = S_z/2$
f_4	$f_1 \cdot f_2$	$J_4 = (S_x S_y + S_y S_x)/2$
f_5	$f_1 \cdot f_3$	$J_5 = (S_x S_z + S_z S_x)/2$
f_6	$f_2 \cdot f_3$	$J_6 = (S_y S_z + S_z S_y)/2$
f_7	$f_3^2 - f_4^2$	$J_7 = (S_x S_x - S_y S_y)/2$
f_8	$\sqrt{1 - f_3^2} (3 - 4(1 - f_3^2))$	$J_8 = \sqrt{3} (S_z S_z/2 - \mathbb{I}/3)$

The $S_i, i \in \{x, y, z\}$ are the three spin-1 operators, and the J'_i 's matrices have orthonormal properties $\text{Tr}[J_i J_j] = \delta_{ij}/2$, for $i, j > 0$ (3 if $i = j = 0$). For a process where two spin-1 W bosons decay hadronically, the joint angular distribution of the final decayed fermions are

written as [40]

$$\frac{1}{\sigma} \frac{d\sigma}{d\Omega_{j_1} d\Omega_{j_2}} = \sum_{\lambda_{W-}, \lambda'_{W-}, \lambda_{W+}, \lambda'_{W+}} \rho_{W-W+}(\lambda_{W-}, \lambda'_{W-}, \lambda_{W+}, \lambda'_{W+}) \times \Gamma_{W-}(\lambda_{W-}, \lambda'_{W-}) \Gamma_{W+}(\lambda_{W+}, \lambda'_{W+}), \quad (2.1)$$

where the production density matrix ρ_{W-W+} can be written in basis space of 9×9 matrices formed by the tensor product $\{\mathbb{I} \otimes \mathbb{I}, \mathbb{I} \otimes J_i, J_i \otimes \mathbb{I}, J_i \otimes J_j\}$. Then, the density matrix is given by (see for example [40])

$$\rho_{W-W+} = \mathbb{I} \otimes \mathbb{I} + \sum_{i=1}^8 \left(P_i^{(2)} \mathbb{I} \otimes J_i^{(2)} + P_i^{(1)} J_i^{(1)} \otimes \mathbb{I} \right) + \sum_{i,j=1}^8 C_{ij}^{(12)} J_i^{(1)} \otimes J_j^{(2)}. \quad (2.2)$$

Here, P 's are eight independent polarization, and $C_{ij}^{(12)}$ are 64 correlation parameters. These parameters can be obtained from the asymmetries in the correlators as,

$$A_{ij} = \frac{\sigma(f_i^{(1)} f_j^{(2)} > 0) - \sigma(f_i^{(1)} f_j^{(2)} < 0)}{\sigma(f_i^{(1)} f_j^{(2)} > 0) + \sigma(f_i^{(1)} f_j^{(2)} < 0)}, \quad (2.3)$$

where A_{i0} and $A_{0j}, i, j \in 1, 8$, are the polarization asymmetries for W^- and W^+ , respectively. And $A_{ij}, i, j \in \{1, \dots, 8\}$ are the spin correlation asymmetries. The parameters $f_i^{(1/2)}, i \in \{1..8\}$ are the corresponding correlators or angular functions associated with the two distinct final fermions, which are listed in Table 1. One can obtain the exact relation between the asymmetries with polarization, and spin correlation parameters by doing a partial integration of Eq. (2.1) (see Ref. [40]). In Eq. (2.1), the Γ matrices are normalized decay density matrix of W boson given by,

$$\Gamma(\lambda, \lambda') = \begin{bmatrix} \frac{1+\delta+(1-3\delta)\cos^2\theta+2\alpha\cos\theta}{4} & \frac{\sin\theta(\alpha+(1-3\delta)\cos\theta)}{2\sqrt{2}} e^{i\phi} & (1-3\delta)\frac{1-\cos^2\theta}{4} e^{i2\phi} \\ \frac{\sin\theta(\alpha+(1-3\delta)\cos\theta)}{2\sqrt{2}} e^{-i\phi} & \delta + (1-3\delta)\frac{\sin^2\theta}{2} & \frac{\sin\theta(\alpha-(1-3\delta)\cos\theta)}{2\sqrt{2}} e^{i\phi} \\ (1-3\delta)\frac{(1-\cos^2\theta)}{4} e^{-i2\phi} & \frac{\sin\theta(\alpha-(1-3\delta)\cos\theta)}{2\sqrt{2}} e^{-i\phi} & \frac{1+\delta+(1-3\delta)\cos^2\theta}{4} 2\alpha\cos\theta \end{bmatrix}, \quad (2.4)$$

with polar θ and azimuthal angle ϕ obtained at the rest frame of the mother particle. The parameter α is spin analyzing power of final fermion. For the decay of spin-1 boson to two fermions ($V \rightarrow f_1 f_2$) with decay vertex of the form $\bar{f}_1 \gamma^\mu (C_L P_L + C_R P_R) f_2 V_\mu$ with real $C_{L,R}$, α in the rest frame of V takes the form [37]

$$\alpha = \frac{2(C_R^2 - C_L^2) \sqrt{1 + (x_1^2 - x_2^2)^2 - 2(x_1^2 + x_2^2)}}{(C_R^2 + C_L^2) [2 - (x_1^2 - x_2^2)^2 + (x_1^2 + x_2^2)] + 12C_L C_R x_1 x_2}, \quad (2.5)$$

where $x_i = m_i/m_V$. For the decay $W \rightarrow \ell \nu / j_1 j_2$, with $m_\ell = m_\nu = m_j = 0$ and within the SM we have $C_R = 0$ leading to $\alpha = -1$. Similarly, the expression for the parameter δ is obtained from the decay amplitude and is given by [37]

$$\delta = \frac{(c_R^2 + C_L^2) [(x_1^2 + x_2^2) - (x_1^2 - x_2^2)^2] + 4C_L C_R x_1 x_2}{(C_R^2 + C_L^2) [2 - (x_1^2 - x_2^2)^2 + (x_1^2 + x_2^2)] + 12C_L C_R x_1 x_2}, \quad (2.6)$$

	A ₁	A ₂	A ₃	A ₄	A ₅	A ₆	A ₇	A ₈
A ₁	E	O	E	O	E	O	E	E
A ₂	O	E	O	E	O	E	O	O
A ₃	E	O	E	O	E	O	E	E
A ₄	O	E	O	E	O	E	O	O
A ₅	E	O	E	O	E	O	E	E
A ₆	O	E	O	E	O	E	O	O
A ₇	E	O	E	O	E	O	E	E
A ₈	E	O	E	O	E	O	E	E

Figure 3: Schematic representation of polarization and spin-correlation asymmetries, categorized by their CP properties and flavor dependence. Asymmetries shown in red indicate flavor-dependent observables, while those in blue are flavor independent. The symbols labeled with *E* denote CP-even, and those with *O* denote CP-odd asymmetries.

which at the high energy limit goes to zero.

The correlators f_i ’s have distinct transformation properties under CP. For instance, the correlator f_1 is CP-even, while f_2 is CP-odd. The construction of asymmetries associated with vector polarizations, as well as vector–vector and vector–tensor correlations, requires tagging of the decay products of the W bosons. Since we analyze processes corresponding to the W^-W^+ topology, the decay products of the W bosons are identified according to their flavor structure. For hadronic decays, where the final states consist of quark jets, we employ a boosted decision tree (BDT)-based flavor-tagging algorithm to distinguish jets originating from *up*- and *down*-type quarks. In contrast, for fully leptonic decay channels, we assume ideal lepton identification, and no additional flavor-tagging procedure is required.

The complete CP structure together with the flavor dependence of all asymmetries A_{ij} is summarized in Fig. 3. Asymmetries corresponding to CP-even correlators are denoted by “E”, while those associated with CP-odd correlators are denoted by “O”. Flavor-dependent asymmetries, which rely on identifying the decay flavor of the W daughters, are shown in red, whereas flavor-independent ones are indicated in blue. In total, there are 44 CP-even and 36 CP-odd observables, among which 45 are flavor dependent and 35 are flavor independent in the case of a two spin-1 W^-W^+ production process.

In the subsequent sections, we initiate the collider-level analysis, including event selection and flavor tagging, in the fully hadronic WW decay channel.

3 Collider analysis of $e^-e^+ \rightarrow 4j$ events

The dimension-6 Lagrangian given in Eq. (1.3) are implemented in FEYNRULES [41, 42] to obtain UNIVERSAL FEYNRULES OUTPUT [43, 44] (UFO) model for generation of Monte Carlo events. The matrix level events are generated using MADGRAPH5_AMC@NLO v.7.3 [45, 46] (MG5 henceforth) with the UFO model incorporating the five dimension-6 operators. The electroweak input parameters follows that of LEP or α -scheme [47] which uses $\{\alpha_{EW}, G_F, m_Z\}$ as inputs, where the SM input parameters are defined as,

$$\begin{aligned} e &= \sqrt{4\pi\alpha_{EW}}, \quad g = \frac{e}{\cos\theta}, \quad g' = \frac{e}{\sin\theta}, \quad v = \frac{1}{2^{1/4}\sqrt{G_F}}, \\ \sin^2\theta &= \frac{1}{2} \left[1 - \sqrt{1 - \frac{4\pi\alpha_{EW}}{\sqrt{2}G_F m_Z^2}} \right], \quad m_W^2 = m_Z^2 \cos^2\hat{\theta}. \end{aligned} \quad (3.1)$$

The showering of colored partons and hadronization of final state particles are done using PYTHIA v8.3.06 [48]. Finally, the detector effects are implemented with DELPHES [49] with publicly available International Linear Collider (ILC) simulation parameters [50] in DELPHES.

To quantify the size of the interference between the resonant W^-W^+ contribution and the Non- W^-W^+ (QCD and electroweak) topologies, we first generate dedicated event samples using a diagram filter in MG5. The filter removes the resonant W^-W^+ amplitudes, thereby yielding a sample that includes only the non-resonant QCD and electroweak (VV , with $V \in \{Z, \gamma\}$) contributions. This Non- W^-W^+ sample effectively serves as the background to the fully hadronic W^-W^+ signal in $e^-e^+ \rightarrow 4j$ production. The inclusive $4j$ sample, on the other hand, contains all gauge-invariant diagrams contributing to the process, including WW , ZZ , QCD, and their mutual interference, as schematically illustrated in Fig. 1.

At $\sqrt{s} = 250$ GeV, the leading-order cross sections obtained are $\sigma_{WW} = 3.46$ pb, $\sigma_{4j} = 4.19$ pb, and $\sigma_{\text{Non-}WW} = 0.63$ pb. The interference between the W^-W^+ and Non- W^-W^+ amplitudes is found to be small, approximately 0.1 pb, corresponding to about 2.3% of the total $e^+e^- \rightarrow 4j$ cross section when contributions up to $\mathcal{O}(\alpha_{EW}^4 + \alpha_{EW}^3\alpha_S + \alpha_{EW}^2\alpha_S^2)$ are included.

To further characterize the dominant background topologies and to study the performance of event classification techniques, we simulate four distinct samples: (i) the inclusive $4j$ process containing all gauge-invariant contributions, (ii) the pure electroweak $W^-W^+ \rightarrow 4j$ process, representing the signal, (iii) the pure electroweak $ZZ \rightarrow 4j$ process and (iv) the QCD-like $4j$ process. All events are generated at a center-of-mass energy of 250 GeV with the following parton-level kinematic selections:

$$p_T^j \geq 20.0 \text{ GeV}, \quad \max(|\eta_j|) = 5.0, \quad \min(\Delta R_{ja,jb}) = 0.4, \quad (3.2)$$

where η_j is the pseudorapidity of jets and $\Delta R_{ja,jb} = \sqrt{(\eta_{ja} - \eta_{jb})^2 + (\phi_{ja} - \phi_{jb})^2}$ is the geometric distance between two jets.

Events are required to contain at least four reconstructed jets. Figure 4 shows the reconstructed jet multiplicity and the invariant mass distributions of leading jet pairs for the

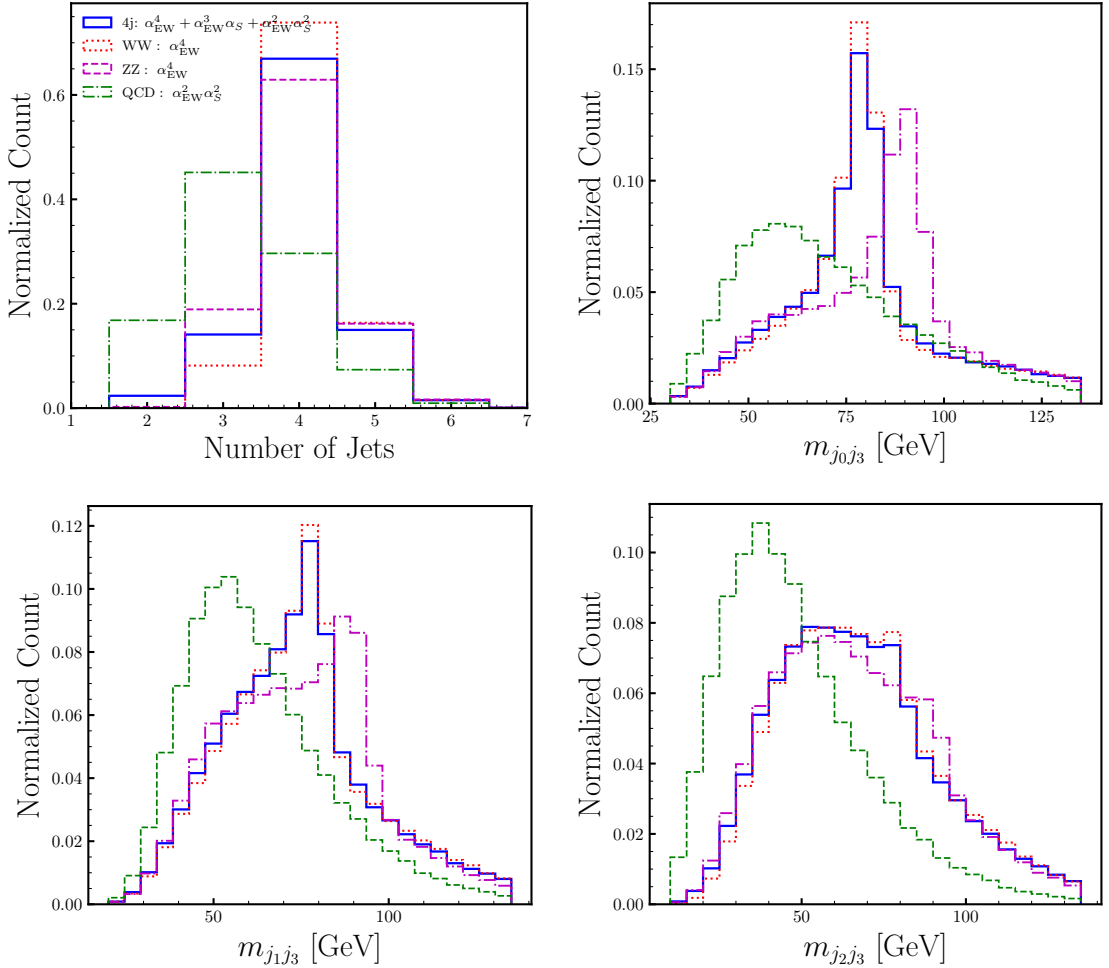


Figure 4: Detector level distribution of number of jets and invariant mass of pair of jets for four different processes at $\sqrt{s} = 250$ GeV. The distribution are obtained for $e^-e^+ \rightarrow 4j$ process along with di-boson (W^-W^+ , ZZ) and QCD production. The detector analysis is achieved with simulation with ILC detector implemented in DELPHES.

different process categories. These samples form the basis for the subsequent multivariate classification, where a boosted decision tree (BDT) is employed to distinguish the W^-W^+ signal from the dominant ZZ and QCD backgrounds.

3.1 Event selection with boosted decision trees

To distinguish between WW , ZZ , and QCD-induced four-jet topologies, we employ a gradient-boosted decision tree multi-class classifier. The input feature set, detailed in Table 2, comprises kinematic observables constructed from the four leading jets: transverse momenta ($p_T^{j_i}$, $i \in \{0, 1, 2, 3\}$), rapidities (η_{j_i}), azimuthal angles (ϕ_{j_i}), dijet invariant masses ($m_{j_a j_b}$), dijet transverse momentum sums ($p_T^{j_a j_b}$), angular separations ($\Delta R_{j_a j_b}$), the scalar sum of all jet transverse momenta (H_T), the four-jet invariant mass (m_{4j}), and jet charge observables (Q_j^κ) computed with varying κ exponents.

Table 2: List of observables used as an input features for boosted decision tree in order to classify signal vs. background events. The features are derived at $\sqrt{s} = 250$ GeV at the detector (DELPHES) level.

Features	Description	Features	Description
$p_T^{j_i}, i \in \{0, \dots, 3\}$	p_T of four leading jets	η_{j_i}	Pseudorapidity of jets
ϕ_{j_i}	Azimuth orientation of jets	p_T^j	Scalar sum of p_T of all jets
m_j	Invariant mass of all jets	$p_T^{j_a, j_b}$	Scalar sum of p_T two jets
m_{j_a, j_b}	Invariant mass of two jets	$\Delta R_{j_a, j_b}$	Geometric distance
Q_J^k	Jet charge with different k		

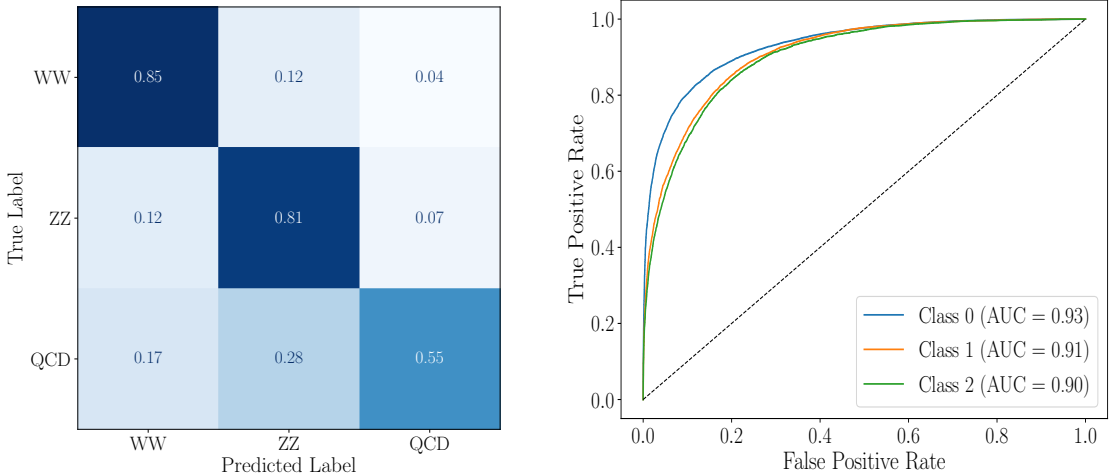


Figure 5: We show the confusion matrix and ROC curves to highlight the efficiency of network to classify signal events (W^+W^-) from the ZZ and QCD backgrounds.

Hyperparameter tuning is performed via exhaustive grid search with three-fold cross-validation, minimizing the multi-class logarithmic loss. The optimal configuration consists of: maximum tree depth = 8, learning rate $\eta = 0.05$, number of estimators = 500, and sub-sample ratio = 0.7. Input features are preprocessed using mean imputation for missing values and standard scaling to zero mean and unit variance. The model employs the MULTI:SOFTPROB objective function to output calibrated class probabilities for the three event categories.

The trained classifier achieves robust discrimination between the WW signal and backgrounds (ZZ and QCD), as quantified by the confusion matrix and one-versus-rest receiver operating characteristic (ROC) curves presented in Fig. 5. The confusion matrix demonstrates that WW events are correctly identified with 85% efficiency (true positive rate), while background contamination remains modest: 12% of WW events are misclassified as

ZZ and only 4% as QCD. The dominant confusion with ZZ backgrounds is expected, as both processes yield diboson topologies with similar jet multiplicity and kinematic distributions, differing primarily in the invariant mass reconstructions of the decay products. Conversely, Non- WW events are misidentified as follows: 12% of ZZ and 17% of QCD events leak into the WW category (background events), resulting in an improved signal purity ($P = N_S/(N_S + N_B)$) that must be accounted for in subsequent sensitivity analyses. In particular, the signal purity P increases from $\approx 86\%$ to 97% on using multi-variate classifier.

The *one-versus-rest* ROC analysis quantifies the WW signal-background separation power through the area under the curve (AUC). The WW classifier achieves $AUC_{WW} = 0.93$, indicating excellent discrimination against the combined ZZ and QCD backgrounds. This high AUC value reflects the classifier’s ability to exploit the characteristic dijet mass structure of W boson decays ($m_W \approx 80$ GeV) in conjunction with angular observables and jet charge asymmetries. For comparison, the background classifiers yield $AUC_{ZZ} = 0.91$ and $AUC_{QCD} = 0.90$, demonstrating that the multi-class approach successfully disentangles all three topologies.

To assess the stability of the classifier under finite sample variations, we perform a bootstrap analysis by computing the overall accuracy on randomly selected 40% subsets of the test data over 1000 iterations. This procedure yields a mean accuracy of $(78.0 \pm 0.5)\%$, demonstrating robust and stable predictive performance. The small standard deviation confirms that the classifier generalizes well and is not sensitive to particular test sample compositions.

3.2 Reconstruction of oppositely charged two W bosons

Once the WW -like events are tagged, the next question to tackle is to figure out which pair of jets is more closely W^- or W^+ aligned. This W tagging is necessary in order to reconstruct the polarization and spin correlations of two W bosons. From the kinematic consideration, it becomes extremely difficult to tag the jet pair to respective charge as the hadronization of decayed quarks from two oppositely charged W bosons are similar leading to similar jet kinematic structure.

To discriminate between jets originating from W^- and W^+ decays, we employ the p_T -weighted *jet charge* observable [51, 52], defined as

$$Q_J^\kappa = \frac{1}{p_{TJ}^\kappa} \sum_{i=1}^n Q_i p_{Ti}^\kappa, \quad (3.3)$$

where p_{TJ} is the transverse momentum of the jet, and Q_i and p_{Ti} denote the electric charge and transverse momentum of its constituents, respectively. The exponent κ is a phenomenological parameter that controls the relative weight of soft and hard constituents, typically chosen in the range $0 \leq \kappa \leq 1$.

To quantify the discriminating power of Q_J^κ , we simulate two semi-leptonic $e^-e^+ \rightarrow W^-W^+ \rightarrow jj(\ell^\pm\nu_\ell)$ processes, along with the inclusive $e^-e^+ \rightarrow 4j$ process. The latter is generated with a diagram filter that removes the W^-W^+ resonant amplitudes, ensuring

that only non-resonant QCD and electroweak (VV , $V \in \{Z, \gamma\}$) topologies contribute and act as background to full-hadronic channel. We focus on the semi-leptonic channels to avoid the combinatorial ambiguity associated with pairing jets in the fully hadronic final state. All events are generated at $\sqrt{s} = 250$ GeV using MG5, followed by parton showering and hadronization with PYTHIA, and detector simulation with DELPHES.

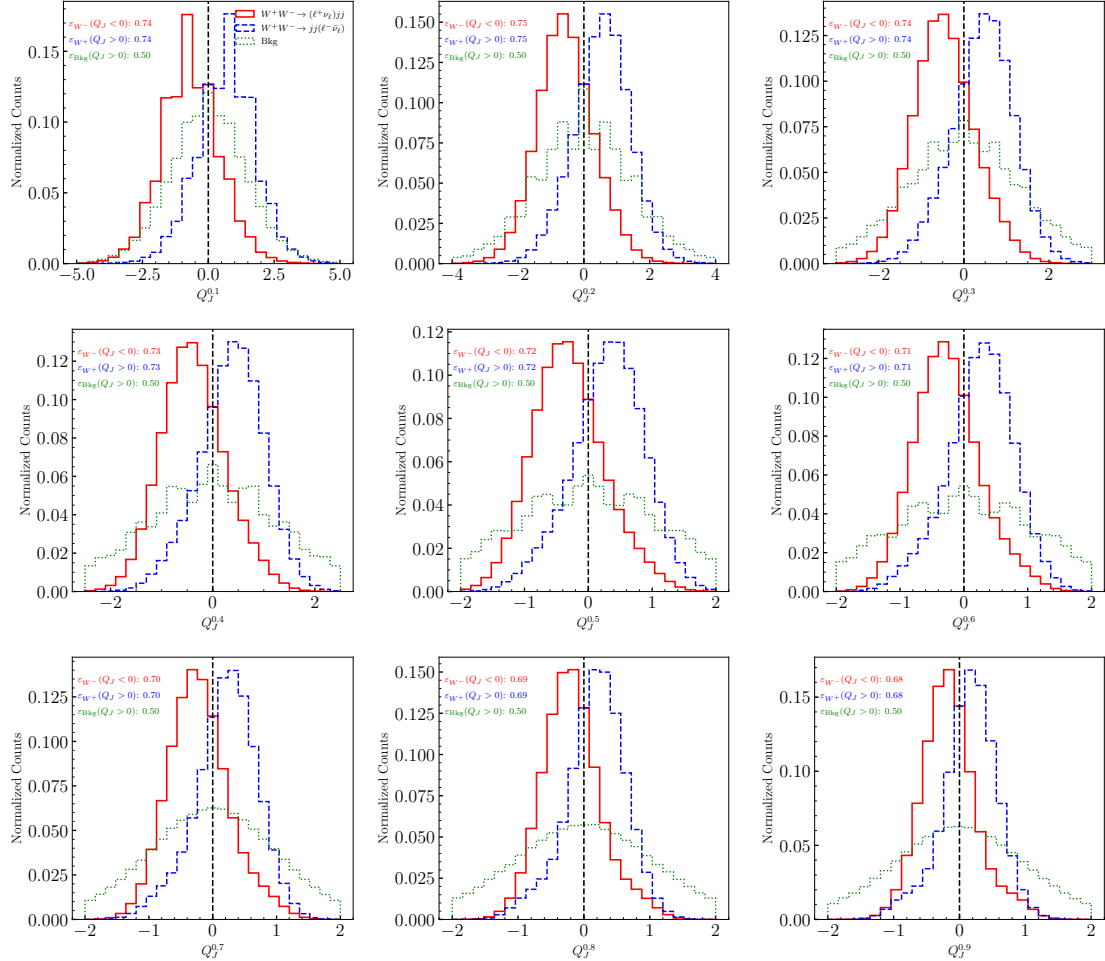


Figure 6: Normalized distribution of jet charge variable for two different semi-leptonic decay of WW di-boson process and background events for four jet events. The distribution are obtained at the level of detector implemented in DELPHES at $\sqrt{s} = 250$ GeV.

In Fig. 6, we show the normalized distributions of Q_J^κ for various κ values across the three processes. A clear charge asymmetry is observed between the two semi-leptonic WW channels, while the $4j$ background remains symmetric around zero. This symmetry indicates that Q_J is an effective discriminator only for resonant WW topologies. The best tagging performance is achieved for $\kappa = 0.2$, yielding a tagging efficiency of approximately 0.75.

In the fully hadronic $e^-e^+ \rightarrow 4j$ case, the main challenge arises from the combinatorial ambiguity in pairing jets into W candidates. Let $J_i \in \{J_1, J_2, J_3, J_4\}$ denote

the four leading jets. Three distinct pairings can be formed: $P_1 = \{(J_1, J_2), (J_3, J_4)\}$, $P_2 = \{(J_1, J_3), (J_2, J_4)\}$, and $P_3 = \{(J_1, J_4), (J_2, J_3)\}$. We select the pairing for which the product of the two jet charges is negative. If multiple pairings satisfy this condition, the one minimizing $\|m_{J_i} - m_W\| + \|m_{J_j} - m_W\|$ is chosen.

For the $e^-e^+ \rightarrow 4j$ analysis, we employ $Q_j^{0.2}$, assuming the same optimal κ value applies as in the semi-leptonic case, since the observable primarily probes jet substructure, which is expected to be similar in both topologies. The jet pair with negative (positive) total charge is identified as the W^- (W^+) candidate.

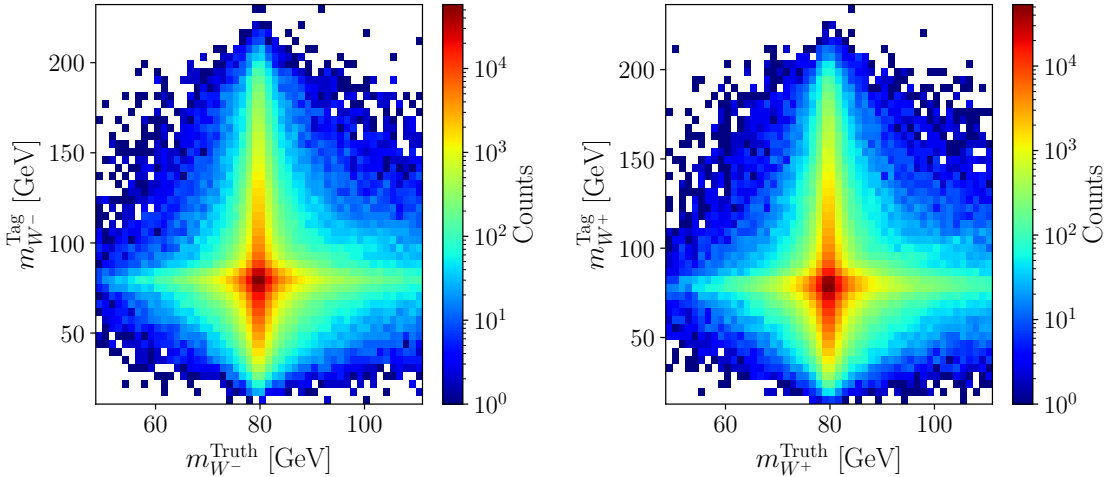


Figure 7: Two dimensional distribution of invariant mass of W bosons at the level of reconstruction and parton level. The distribution are obtained for full-hadronic decay of W^-W^+ di-boson process at e^-e^+ collider at $\sqrt{s} = 250$ GeV.

Figure 7 shows the correlation between the reconstructed and parton-level invariant masses of the charged W bosons for the fully hadronic $e^-e^+ \rightarrow 4j$ process. For roughly 80% of the events, the reconstructed W mass deviates from the parton-level value by less than 20 GeV. A vertical condensation pattern is visible, which reflects fluctuations in the reconstructed jet energies. A similar feature is also observed in the semi-leptonic channel (not shown here), suggesting that the spread originates mainly from hadronization and detector effects rather than from incorrect jet pairing. Once the charged W^\pm bosons are successfully tagged, we proceed to identify the flavor of their daughter jets in the subsequent analysis.

3.3 Decision trees based flavor tagging of W^\pm jets

The endeavor of jet tagging, which involves identifying the origin of jets produced in high-energy collisions, has been a pivotal aspect of particle physics research. Historically, significant attention was directed towards distinguishing quark-initiated jets from gluon-initiated jets, leveraging the inherent differences in their color charge and associated radiation patterns [53]. The Altarelli-Parisi splitting functions elucidate that gluons, characterized by a higher color factor ($C_A = 3$) compared to quarks ($C_F = 4/3$), tend to radiate more,

resulting in jets with a higher constituent multiplicity and broader radiation patterns. This foundational understanding was instrumental in early experimental investigations conducted by different collaborations such as SLAC [54–56], JADE [57, 58], TASSO [59], AMY [60], DELPHI [61], and OPAL [62, 63].

At lower energy scales, the structural similarities between gluon jets and b -jets, particularly in terms of constituent multiplicity due to the extended decay chains of B -hadrons [64], posed challenges in differentiation. However, at the Large Hadron Collider (LHC), the higher transverse momenta (p_T) have accentuated the distinctions between gluon and b -jets, primarily due to the increased color activity inherent in Quantum Chromodynamics (QCD) processes. These color properties had been utilized in ATLAS [65–67] and CMS [68] for tagging jets initiated by gluons and quarks.

The advent of machine learning (ML) techniques has revolutionized jet tagging methodologies. Initial studies demonstrated that employing multivariate analyses [69], utilizing variables such as charged track multiplicity and p_T -weighted linear radial moments, could achieve performance levels comparable to traditional methods. Subsequent research expanded the repertoire of jet substructure observables, incorporating metrics like Les Houches Angularity, width, thrust, and $(p_T^D)^2$, to enhance tagging accuracy [70]. The jet charge variable has also been studied for tagger purposes [71].

Machine learning has further transformed jet tagging by surpassing traditional feature-based methods through data-driven approaches. Early applications used CNNs to process jets as images, enhancing quark/gluon discrimination and boosted object tagging [72–80]. Graph-based models like PARTICLENET improved performance by representing jets as graphs with kinematic relationships encoded in edges [81]. Transformer models further advanced tagging via self-attention, capturing long-range correlations among jet constituents [81, 82]. Energy Flow Networks (EFNs) introduced a permutation-invariant approach leveraging energy flow polynomials for full kinematic representation [83]. While deep learning dominates, BDTs remain crucial for fast, interpretable classification in real-time event selection [84]. Unsupervised and weakly supervised methods reduce dependence on labeled data, utilizing Poissonian likelihood-based tagging and weak supervision [85, 86]. Likelihood discriminants remain a key traditional tool [87], while DEEPJET integrates diverse jet features to boost efficiency [88]. Among ML architectures, transformers currently achieve the highest classification accuracy [81].

In the present analysis, we focus not on the complete quark flavor identification but specifically on distinguishing between *up-type* and *down-type* jets originating from W boson decays. The two leading jets in our events arise from hadronic W decays, and within the SM, these correspond to light-quark (u, d, c, s) initiated jets. Knowledge of whether a jet is *up* or *down*-type becomes essential for reconstructing polarization and spin-correlation observables that probe anomalous $W^-W^+\gamma/Z$ couplings. Without flavor tagging, certain spin-dependent asymmetries would average out, reducing sensitivity [18].

To achieve efficient *up/down* discrimination, we developed a BDT model using the XGBoost framework. Input features were constructed from the jet constituents after identifying the two charged W bosons through jet charge. Table 3 lists the observables used as input features, derived at $\sqrt{s} = 250$ GeV at the detector (DELPHES) level. Continuous

Table 3: List of observables used as input features for the boosted decision tree to classify the two leading jets as either *up/down*-type jets. The features are derived at $\sqrt{s} = 250$ GeV at the detector (**Delphes**) level.

Feature	Description
$N_\gamma, N_\ell, N_{\pi^\pm}, N_{K^\pm}$	Number of $\gamma, \ell^\pm, \pi^\pm$, and K^\pm
$p_\gamma, p_\ell, p_\pi, p_K$	Four-momentum of $\gamma, \ell^\pm, \pi^\pm$, and K^\pm
$p_T^\gamma, p_T^\ell, p_T^{\pi^\pm}, p_T^{K^\pm}$	Scalar sum p_T of respective particles
Q_J^κ	Jet charge ($\kappa \in \{0, 1\}$)
N_d	Count of mother particles with lifetime $d > 0.3$ mm

variables, such as particle momenta, are normalized by the jet energy. We also compute

Table 4: Architecture and hyperparameters of the XGBoost BDT used for W -boson jet flavor classification.

Parameter	Value / Description
Number of trees ($n_{\text{estimators}}$)	1000
Maximum tree depth (<code>max_depth</code>)	5
Learning rate (η)	0.01
Subsample ratio of columns (<code>colsample_bytree</code>)	0.9
Regularization L1 term (α)	1.5
Regularization L2 term (λ)	1.5
Tree splitting criterion	Gradient-based (second-order)
Minimum loss reduction (γ)	1.5
Feature scaling	Min–Max normalization (per feature)
Training–validation–test split	70% : 15% : 15%

the number of mother particles that have traveled a distance $d > 0.3$ mm from the primary vertex. Such particles give rise to displaced tracks, and in the case of c -quark-initiated jets, a significant number of short-lived kaons (K_0^S) contribute to this feature. For training, we used fully hadronic WW decays and assigned truth labels by matching quarks to jets using the geometric distance $\Delta R = \sqrt{\Delta\phi_{qj}^2 + \Delta\eta_{qj}^2}$. Among the four possible quark–jet pairings, the closest pair was chosen; in case of degeneracy, the harder jet was assigned to the quark. The BDT architecture and hyperparameters are summarized in Table 4.

The model was trained on unpolarized datasets, as these yielded performance comparable to polarized samples [18]. Its classification accuracy was evaluated through iterative sub-sampling of test data, achieving approximately 82% mean accuracy with a variance of 0.01%. The distributions of classification accuracy for W^- and W^+ jets are shown in Fig. 8. The trained BDT model is subsequently used to reconstruct the polarization

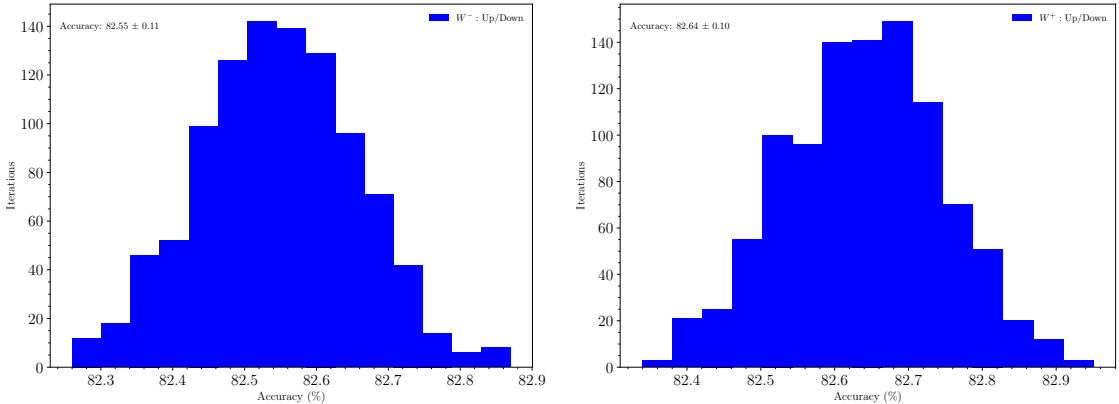


Figure 8: Distribution of accuracy in classifying two leading jets from tagged W bosons as *up/down*-type jets using boosted decision trees.

and spin-correlation asymmetries, which serve as inputs to probe anomalous $W^-W^+\gamma/Z$ couplings in Section 5.

4 Collider analysis of $e^-e^+ \rightarrow \ell^-\ell^+\not{E}$ events

At leading order (LO), the production of final states comprising two oppositely charged leptons and missing transverse energy at an electron-positron collider arises from several distinct classes of Feynman diagrams, as illustrated in Fig. 2. The primary signal process corresponds to W^-W^+ production, where the intermediate states involve both γ/Z -mediated *s*-channel diagrams and ν_e -mediated *t*-channel exchange. These diagrams contribute dominantly to the electroweak di-boson topology and serve as the principal focus of our analysis.

In contrast, the dominant irreducible backgrounds arise from vector boson fusion (VBF) processes, which involve *t*-channel exchange of gauge bosons resulting in final-state leptons and neutrinos, as depicted in the middle row of Fig. 2. In addition, there exists a continuum background arising from non-resonant contributions that mimic the same final state. To enhance the sensitivity to the di-boson signal and reduce contamination from background topologies, we simulate three distinct event samples within our Monte Carlo simulation pipeline (described previously in the context of the four-jet analysis). The first sample includes the complete set of LO amplitudes contributing to the $e^-e^+ \rightarrow \ell^-\ell^+\not{E}$ final state. The second sample isolates only the pure signal processes corresponding to W^-W^+ production. The third sample comprises background-only contributions, excluding all diagrams associated with the di-boson topology. These samples are generated using the diagram filtering capabilities of the MG5 framework.

It is worth emphasizing that the dimension-six operators introduced in the previous section not only modify the W^-W^+ production amplitudes but also contribute anomalously to the VBF processes. As such, VBF topologies may serve as an independent and complementary probe of new physics effects. Nevertheless, in the present study, we re-

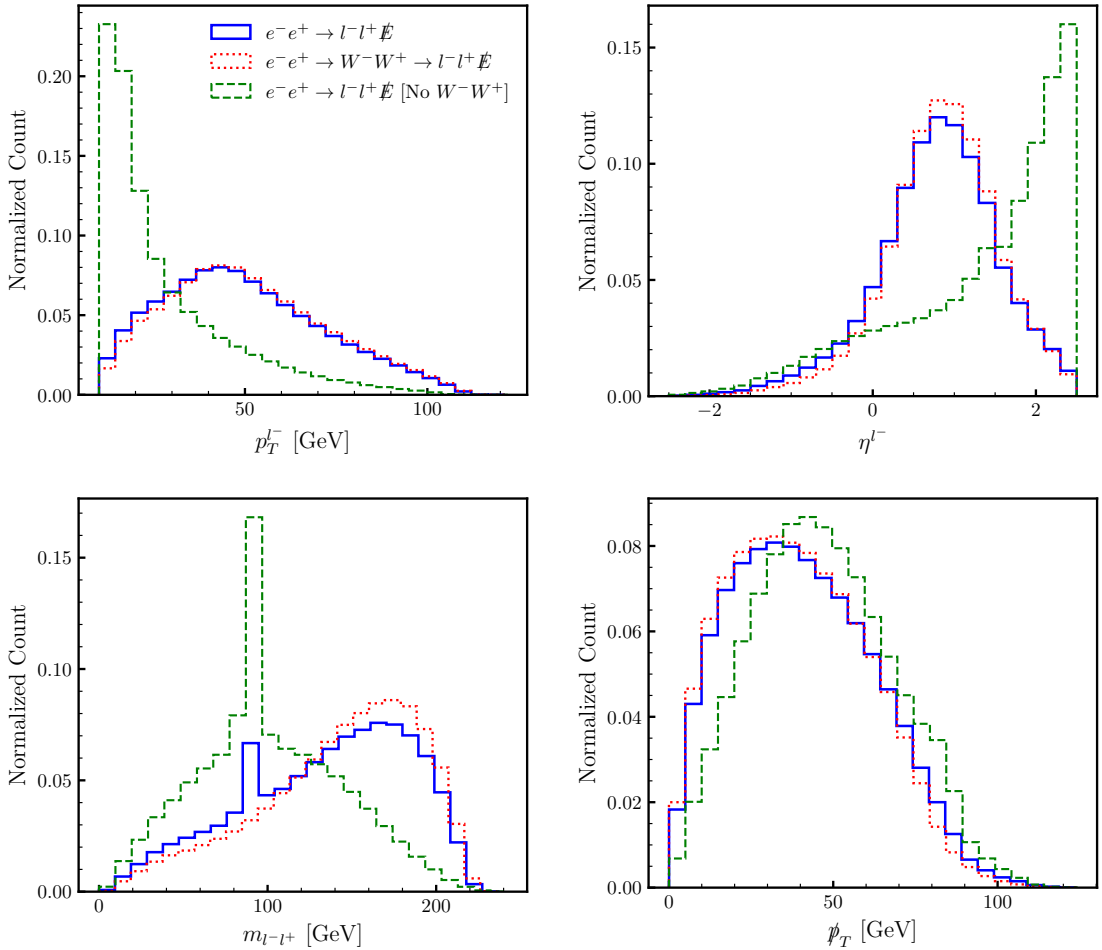


Figure 9: Detector level kinematic distribution of leptons and missing neutrino for $\ell^-\ell^+\not{E}$ events at $\sqrt{s} = 250$ GeV e^-e^+ collider. The distribution are obtained at leading order for three different processes viz. i) complete events $e^-e^+ \rightarrow \ell^-\ell^+\not{E}$, ii) signal events $e^-e^+ \rightarrow W^-W^+ \rightarrow \ell^-\ell^+\not{E}$, and iii) background process devoid of W^-W^+ amplitudes.

strict our attention to the di-boson production channel, while a detailed investigation of VBF-sensitive observables is deferred to future work.

In Fig. 9, we present the normalized detector-level distributions of several kinematic observables constructed from the final-state leptons and the missing transverse momentum at a center-of-mass energy of $\sqrt{s} = 250$ GeV. Among the various observables examined, the transverse momentum of the negatively charged lepton (p_T^-) and the invariant mass of the dilepton system ($m_{\ell-\ell^+}$) exhibit significant discriminating power between the signal and background processes. Specifically, the p_T^- distribution for background events exhibits a peak near 10 GeV, whereas the corresponding distribution for signal events peaks at approximately 50 GeV. Similarly, in the $m_{\ell-\ell^+}$ distribution, the background contribution features a pronounced peak around 90 GeV—consistent with Z -boson mediated processes—while the signal exhibits a broader distribution with a peak around 160 GeV,

reflecting the kinematic features of off-shell W^-W^+ production.

We use cut-based analysis to select the signal rich phase space. Events with two oppositely charged leptons and missing transverse momenta are selected with cuts

$$p_T^{\ell^-} \geq 25 \text{ GeV}, \quad m_{\ell^-l^+} \geq 130.0 \text{ GeV}.$$

Upon applying the selection cuts, the signal purity improves from 76% (without cuts) to 95%. Once the events are selected, the next hurdle is the reconstruction of 4-momenta of two missing neutrinos. It is required in order to compute the spin polarizations and correlations asymmetries at the rest frame of mother W bosons. In the current work, we employ the artificial neural network (ANN) to perform a regression algorithm to compute the momenta of two missing neutrinos, which will be described in the next section.

4.1 Reconstruction of two missing neutrinos

A fully connected feed-forward neural network is employed to regress the three-momenta of the two invisible neutrinos in dileptonic W^-W^+ events at lepton colliders. The input features comprise eight kinematic observables corresponding to the four-momenta of the charged leptons, (p_x, p_y, p_z, E) for each of ℓ^- and ℓ^+ along with p_T, η and ϕ of two charged leptons. Additional features used are $\Delta R_{\ell^-\ell^+}, m_{\ell^-\ell^+}, m_T^{\ell^-\ell^+}, \not{p}_T$ and $\not{\Phi}$. Here, \not{p}_T denotes the missing transverse momentum, and $\not{\Phi} = \tan^{-1}(\not{p}_y/\not{p}_x)$ [89] represents the azimuthal orientation of the missing energy in the transverse plane. The transverse plane is defined perpendicular to the beam axis, with the $\Phi = 0$ direction lying in the x - z plane, which corresponds to the production plane of the W^- boson. The targets are the six momentum components (p_x, p_y, p_z) of the neutrino and antineutrino. The network consists of three hidden layers with 256, 128, and 64 neurons, respectively. Each layer is followed by batch normalization, RELU activation, and dropout with probability $p = 0.2$. The output layer is a fully connected linear map to six nodes. The model is trained using the Adam optimizer with learning rate 10^{-3} , minimizing a custom loss function defined as

$$\mathcal{L} = \text{MSE}(\vec{p}^{\text{pred}}, \vec{p}^{\text{true}}) + \alpha \text{MSE}(p_z^{\text{pred}}, p_z^{\text{true}}), \quad \alpha = 2.0, \quad (4.1)$$

where the second term imposes enhanced penalization on deviations in the longitudinal momentum components.

The dataset, consisting of 10^6 events, is randomly partitioned into training and test subsets in an 80:20 ratio. Training is performed using mini-batches of size 256. The quality of the network's predictions is first assessed through two-dimensional correlation plots between the true and predicted neutrino momentum components, as shown in Fig. 10. To further evaluate the impact of the reconstruction on physical observables, we examine angular distributions sensitive to the polarization and spin correlations of the intermediate W bosons, presented in Fig. 11.

In particular, we study the distribution of $\cos \theta^{\ell^-}$, which probes the longitudinal polarization of the W^- boson, and the $\cos \theta \cos \phi$ distribution, sensitive to the P_{xz} component of the tensor polarization of the W^+ boson. Additionally, we consider angular functions corresponding to two distinct tensor-tensor spin correlation structures between the W^-

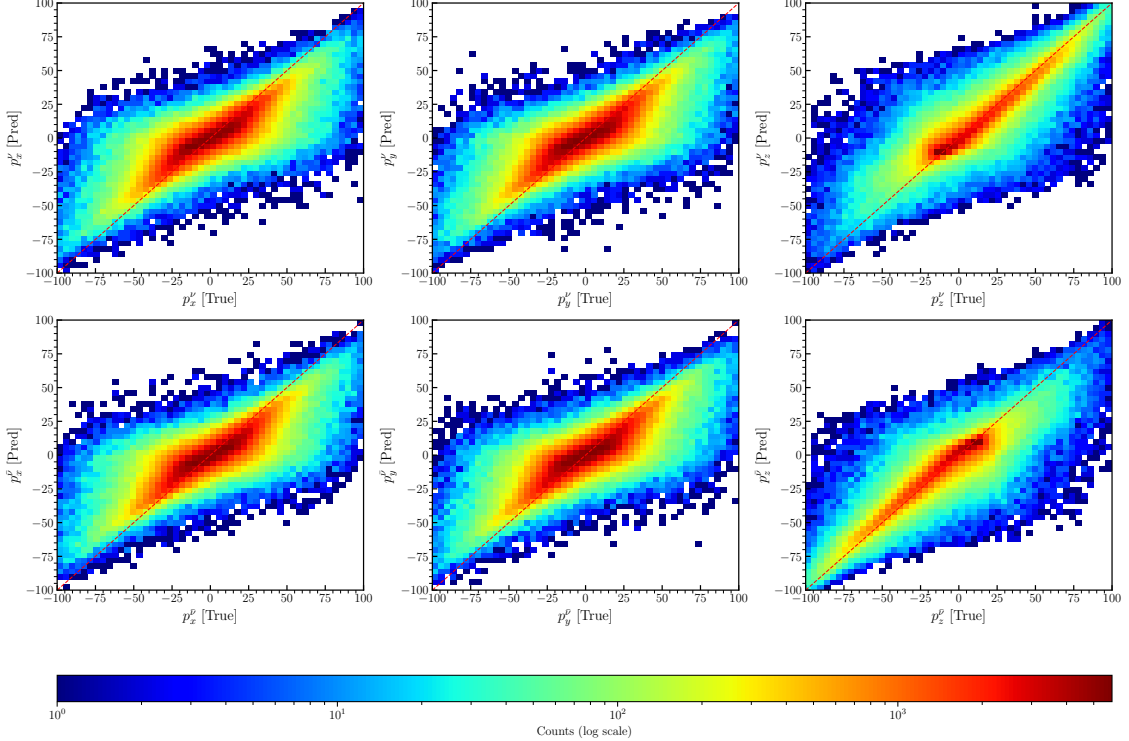


Figure 10: Two dimensional correlation plots for true and predicted three momenta of two missing neutrinos.

and $W+$ bosons. Among these observables, the $\cos \theta^{\ell^-}$ distribution exhibits a noticeable migration of events toward the extreme forward region after reconstruction, which can affect the corresponding polarization asymmetry. The remaining angular observables show good agreement between the truth-level and reconstructed-level distributions, indicating that the neural network preserves the key spin-correlation structures of the underlying process.

5 SMEFT analysis

This section discusses the methodology employed to constrain the anomalous couplings c_i . As discussed in the above section, 16 polarization and 64 spin-correlation asymmetries exist in the case of pair produced W boson. In order to effectively constrain the anomalous couplings, we have categorized all observables into eight distinct intervals of $\cos \theta^{W^-}$, where θ^{W^-} represents the production angle of the W^- boson in the laboratory frame. Within each bin, we have identified 1 cross-section, 16 polarizations, and 64 spin-correlations asymmetries, resulting in a total of 648 observables. These observables have been computed for the SM and several benchmark anomalous points. For each bin of SM and anomalous points, we construct different 648 observables, and these values are used for numerical fitting to obtain a semi-analytical relation between those observables and anomalous couplings. For

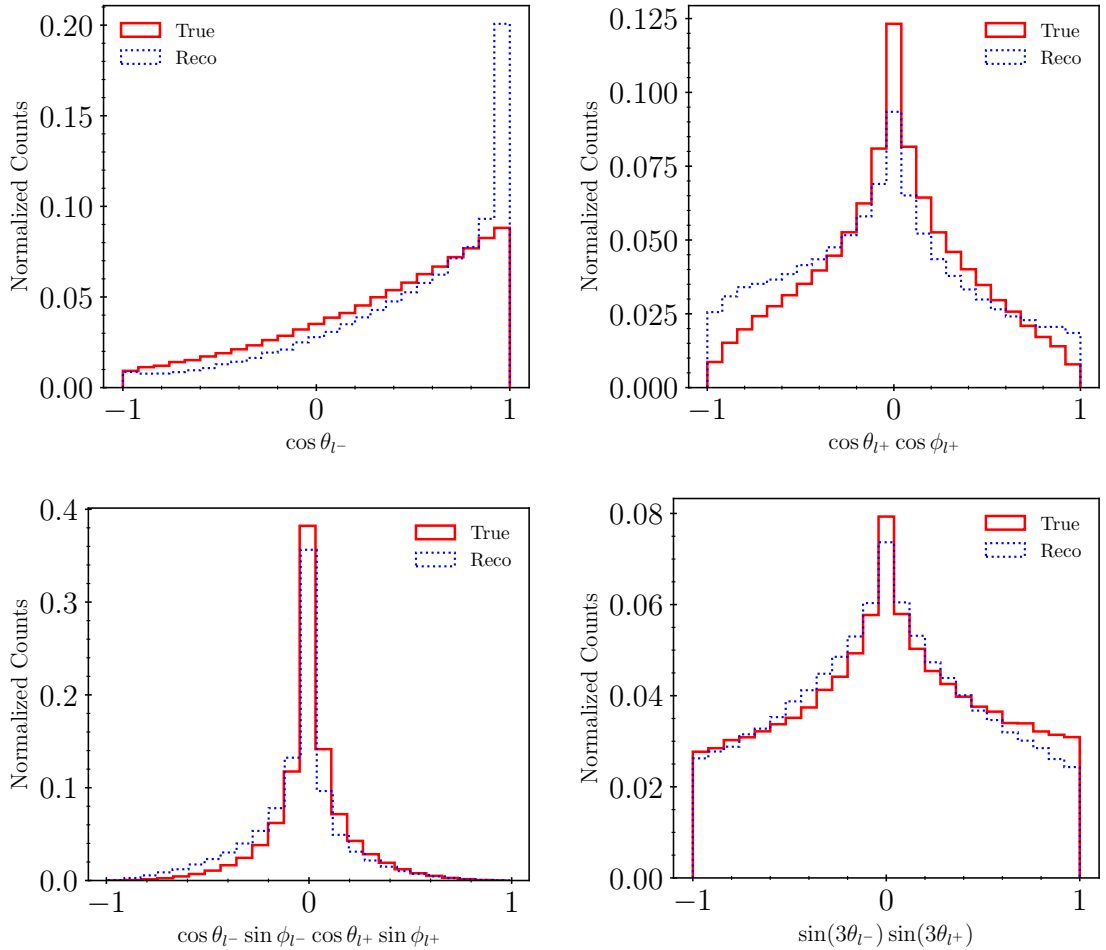


Figure 11: Normalized angular distribution of final leptons at the level of parton truth and reconstructed level. The polar (θ) and azimuth (ϕ) orientation are obtained in the rest frame of W^\pm boson. The reconstruction is done using multi layer perceptron described in main text.

cross section, which is a CP-even observable, the following parametric function is used,

$$\sigma(\{c_i\}) = \sigma_0 + \sum_{i=1}^3 \sigma_i c_i + \sum_{j=1}^5 \sigma_{jj} c_j^2 + \sum_{i>j}^3 \sigma_{ij} c_i c_j + \sigma_{45} c_4 c_5, \quad (5.1)$$

where couplings $c_i \in \{c_1, c_2, c_3\}$ corresponds to CP-even and $c_i \in \{c_4, c_5\}$ corresponds to CP-odd couplings. In the case of asymmetries, the denominator is cross section, while the numerator corresponds to difference in cross section. While fitting the asymmetries (\mathcal{A}), we construct a cross section weighted function, with numerator is defined as $\Delta\sigma = \mathcal{A} \times \sigma$ and the denominator is simply the cross section. The numerator of the CP-odd asymmetries

are fitted using the function,

$$\Delta\sigma(\{c_i\}) = \sum_{i=4}^5 \sigma_i c_i + \sum_{i=1} \sigma_{i4} c_i c_4 + \sum_{i=1} \sigma_{i5} c_i c_5, \quad (5.2)$$

while the CP-even numerator are parameterize using Eq. (5.1).

We study the sensitivity of cross section, polarization asymmetries, and spin correlation asymmetries by constructing the $\Delta\chi^2$ as a function of anomalous couplings. For an observable \mathcal{O} , we find the chi-squared distance between the SM and SM plus anomalous point in the presence of two sets of beam polarization, $(\mp\eta_3, \pm\xi_3)$ as,

$$\begin{aligned} \Delta\chi^2(\mathcal{O}, c, \pm\eta_3, \mp\xi_3) = & \sum_{i,j} \left[\left(\frac{\mathcal{O}_j^i(c, +\eta_3, -\xi_3) - \mathcal{O}_j^i(0, +\eta_3, -\xi_3)}{\delta\mathcal{O}_j^i(0, +\eta_3, -\xi_3)} \right)^2 \right. \\ & \left. + \left(\frac{\mathcal{O}_j^i(c, -\eta_3, +\xi_3) - \mathcal{O}_j^i(0, -\eta_3, +\xi_3)}{\delta\mathcal{O}_j^i(0, -\eta_3, +\xi_3)} \right)^2 \right], \end{aligned} \quad (5.3)$$

where indices i, j represent observables and bins, respectively. The $\delta\mathcal{O}$ is the estimated error on observable \mathcal{O} , for the cross section it is,

$$\delta\sigma = \sqrt{\frac{\sigma}{\mathcal{L}} + (\epsilon_\sigma\sigma)^2}, \quad (5.4)$$

and for various asymmetries, the error is given by

$$\delta\mathcal{A} = \sqrt{\frac{1 - \mathcal{A}^2}{\mathcal{L}\sigma} + \epsilon_\mathcal{A}^2}. \quad (5.5)$$

Here ϵ_σ and $\epsilon_\mathcal{A}$ are the fractional systematic error in cross section σ and asymmetries \mathcal{A} , respectively and σ and \mathcal{L} are the SM cross section and integrated luminosity.

We perform a quantitative comparison of the cross-section sensitivity across the $4j$, $\ell^-\ell^+\not{E}$, and $2j\ell\not{E}$ [17, 18] channels, before examining the role of spin asymmetries in the global sensitivity budget. The normalized cross sections for the unbinned scenario, expanded to quadratic order in the WCs as in Eq. (5.1), are given by

$$\begin{aligned} \frac{\sigma}{\sigma_0}[4j] = & 1.0 - 2.241 \times 10^{-5} c_{WWWW} + 1.353 \times 10^{-3} c_W + 2.874 \times 10^{-4} c_B \\ & + 2.69 \times 10^{-6} c_{WWWW}^2 + 2.781 \times 10^{-5} c_W^2 + 2.216 \times 10^{-6} c_B^2 \\ & + 3.199 \times 10^{-6} c_{\widetilde{W}WW}^2 + 4.938 \times 10^{-6} c_{\widetilde{W}}^2 + 4.955 \times 10^{-5} c_{WWWW} c_W \\ & - 3.371 \times 10^{-5} c_{WWWW} c_B + 3.011 \times 10^{-5} c_W c_B - 2.469 \times 10^{-5} c_{\widetilde{W}WW} c_{\widetilde{W}}, \end{aligned} \quad (5.6)$$

$$\begin{aligned} \frac{\sigma}{\sigma_0}[\ell^-\ell^+\not{E}] = & 1.0 + 4.82 \times 10^{-5} c_{WWWW} + 1.059 \times 10^{-3} c_W + 1.33 \times 10^{-4} c_B \\ & + 1.145 \times 10^{-5} c_{WWWW}^2 + 2.844 \times 10^{-5} c_W^2 + 1.339 \times 10^{-5} c_B^2 \\ & + 1.035 \times 10^{-5} c_{\widetilde{W}WW}^2 + 1.248 \times 10^{-5} c_{\widetilde{W}}^2 - 1.932 \times 10^{-4} c_{WWWW} c_W \end{aligned}$$

$$- 1.935 \times 10^{-4} c_{WWW} c_B - 2.189 \times 10^{-4} c_W c_B - 2.231 \times 10^{-4} c_{\widetilde{W}WW} c_{\widetilde{W}}, \quad (5.7)$$

$$\begin{aligned} \frac{\sigma}{\sigma_0}[2j\ell\bar{E}] = & 1.0 + 4.843 \times 10^{-4} c_{WWW} + 1.347 \times 10^{-3} c_W + 2.525 \times 10^{-3} c_B \\ & + 2.672 \times 10^{-5} c_{WWW}^2 + 1.97 \times 10^{-5} c_W^2 + 7.968 \times 10^{-7} c_B^2 \\ & + 3.172 \times 10^{-5} c_{\widetilde{W}WW}^2 + 4.709 \times 10^{-7} c_{\widetilde{W}}^2 + 1.88 \times 10^{-5} c_{WWW} c_W \\ & + 1.783 \times 10^{-6} c_{WWW} c_B + 6.423 \times 10^{-6} c_W c_B \\ & - 5.326 \times 10^{-6} c_{\widetilde{W}WW} c_{\widetilde{W}}. \end{aligned} \quad (5.8)$$

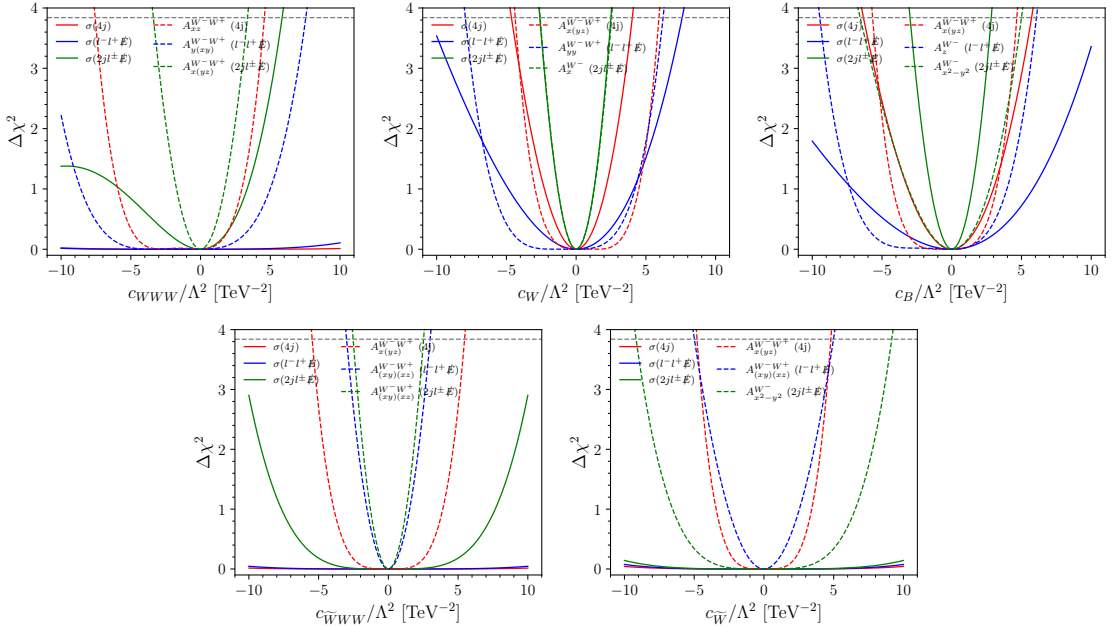


Figure 12: Comparison of sensitivities of cross section and dominant asymmetries for each Wilson coefficient in three different decay channel. The distribution are obtained at $\sqrt{s} = 250$ GeV and $\mathcal{L} = 100$ fb $^{-1}$.

The linear c_{WWW} coefficient in Eq. (5.6) exhibits destructive interference in the $4j$ versus constructive interference in $\ell^- \ell^+ \bar{E}$ and $2j\ell\bar{E}$ channels. The $4j$ channel dominates linear sensitivity for c_W and c_B , establishing interference-level primacy for these WCs. However, the semileptonic channel exhibits exceptional c_B sensitivity (2.525×10^{-3}) which is an order-of-magnitude larger within the interference level in comparison to other two channels. The CP-odd WCs $c_{\widetilde{W}WW}$ and $c_{\widetilde{W}}$ enter cross section purely quadratically at leading order. This quadratic scaling yields intrinsically weaker rate sensitivity compared to CP-even coefficients, requiring CP-sensitive angular observables for optimal constraints.

Asymmetry observables provide superior $\Delta\chi^2$ gradients compared to rate measurements, compensating for statistical disadvantages in channels with smaller cross sections, see Fig. 12. The channel-dependent sensitivity arises from distinct helicity amplitude structures in each final state topology. For c_{WWW} constraints, the $4j$ channel exploits $A_{xz}^{W^-W^+}$

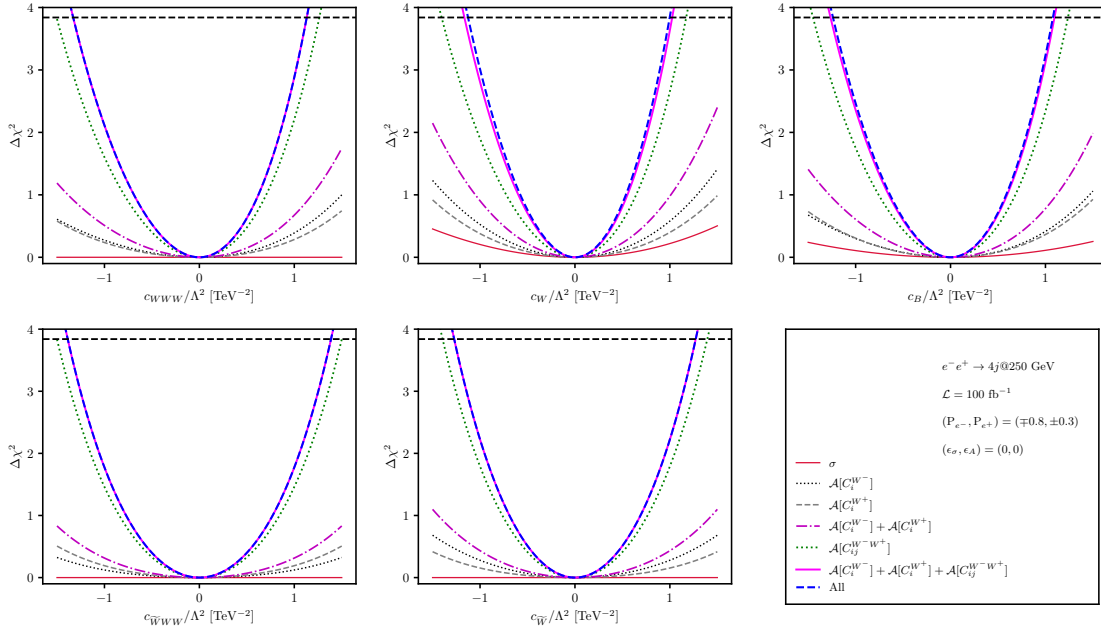


Figure 13: Chi-squared distribution for cross section (σ), polarization asymmetries of two W boson ($\mathcal{A}[C_i^{(W^-/W^+)}]$), spin correlation asymmetries ($\mathcal{A}[C_{ij}^{W^-W^+}]$) and their combinations as a function of one anomalous couplings at a time. The analysis is done for $e^-e^+ \rightarrow 4j$ process at $\sqrt{s} = 250$ GeV, $\mathcal{L} = 100 \text{ fb}^{-1}$ with two set of beam polarization, $(P_{e^-}, P_{e^+}) = (\mp 0.8, \pm 0.3)$, and zero systematic errors. The horizontal line at $\Delta\chi^2 = 3.84$ represent limit on anomalous couplings at 95% CL. The details of legends and working parameters are given on right most panel of bottom row.

vector correlations between W polarizations, while $\ell^-\ell^+\not{E}$ utilizes the diagonal $A_{yy}^{W^-W^+}$ component with superior lepton angular reconstruction. The semileptonic channel maximizes off-diagonal $A_{x(yz)}^{W^-W^+}$ correlations through mixed hadronic-leptonic kinematics. Each asymmetry exhibits steeper $\Delta\chi^2$ slopes than the corresponding rate curves. For the c_W coefficient, the cross-section analysis predicts comparable linear sensitivity across channels ($\mathcal{O}(10^{-3})$), with the hadronic channel maintaining slight advantage. However, the asymmetry contributions fundamentally alter the constraint hierarchy. The $4j$ channel achieves optimal sensitivity through the $A_{W^-}^y$ transverse asymmetry. The $\ell^-\ell^+\not{E}$ channel relies on $A_{W^-}^{x^2-y^2}$, exploiting the clean lepton momentum reconstruction to access azimuthal correlations. And, for the semileptonic channel, dominant contribution to $\Delta\chi^2$ in terms of spin observables comes from $A_{W^-}^x$ component. For c_B , the semileptonic (x^2-y^2) asymmetry of W^- boson combines with the large linear coefficient (2.525×10^{-3}) to create significant enhancement, followed by asymmetry in $x-yz$ correlations in $4j$ channel. The fully leptonic A_z longitudinal asymmetry provides least sensitivity. The CP-odd $c_{\widetilde{W}}$ constraints rely entirely on asymmetry sensitivity due to quadratic-only rate dependence. The $4j$ channel probes $A_{x(yz)}^{W^-W^+}$ through hadronic angular distributions, $\ell^-\ell^+\not{E}$ maintains $A_{yy}^{W^-W^+}$ sensitivity, and $2j\ell\not{E}$ captures (x^2-y^2) azimuthal correlations between decay planes. The

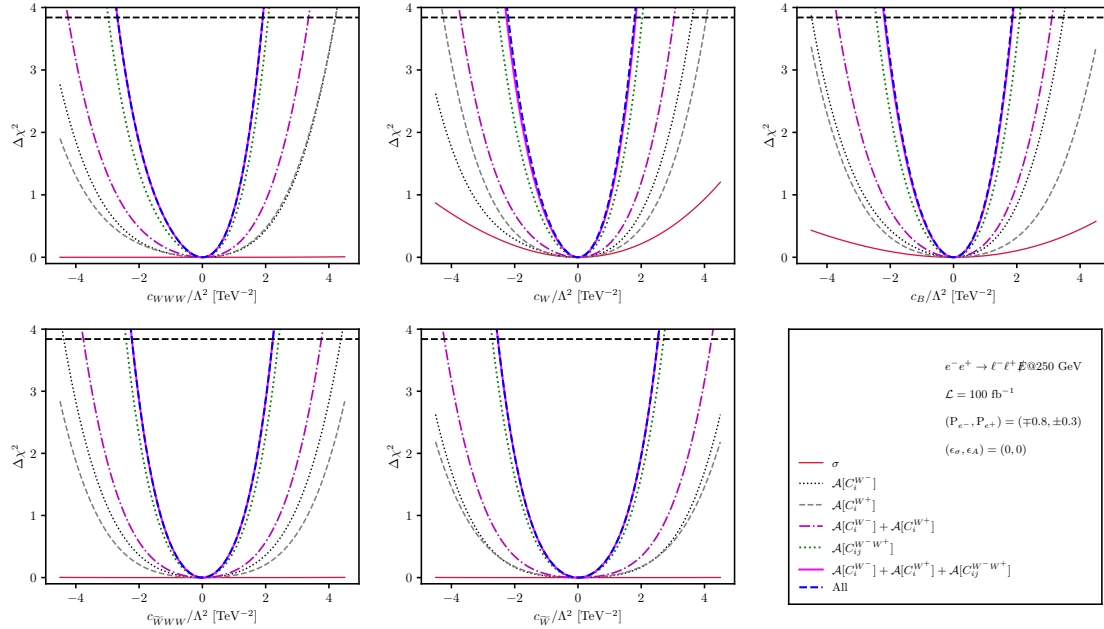


Figure 14: Chi-squared distribution for cross section (σ), polarization asymmetries of two W boson ($\mathcal{A}[C_i^{(W^-/W^+)}]$), spin correlation asymmetries ($\mathcal{A}[C_{ij}^{W^-W^+}]$) and their combinations as a function of one anomalous couplings at a time. The analysis is done for $e^-e^+ \rightarrow \ell^-\ell^+\not{E}$ process at $\sqrt{s} = 250$ GeV, $\mathcal{L} = 100 \text{ fb}^{-1}$ with two set of beam polarization, $(P_{e-}, P_{e+}) = (\mp 0.8, \pm 0.3)$, and zero systematic errors. The horizontal line at $\Delta\chi^2 = 3.84$ represent limit on anomalous couplings at 95% CL. The details of legends and working parameters are given on right most panel of bottom row.

Table 5: 95% CL one parameter limits of WCs obtained using cross section and asymmetries for three different decay channel and also their combinations. The limits are obtained at $\sqrt{s} = 250$ GeV with $\mathcal{L} = 100 \text{ fb}^{-1}$ for each channels at zero systematics.

WCs	$e^-e^+ \rightarrow 4j$	$e^-e^+ \rightarrow \ell^-\ell^+\not{E}$	$e^-e^+ \rightarrow 2j\ell\not{E}$ [18]	Combined
c_{WWW}/Λ^2	$[-1.33, +1.13]$	$[-2.68, +1.91]$	$[-0.93, +0.93]$	$[-0.74, +0.70]$
c_W/Λ^2	$[-1.09, +0.97]$	$[-2.23, +1.80]$	$[-0.63, +0.63]$	$[-0.53, +0.52]$
c_B/Λ^2	$[-1.16, +1.05]$	$[-2.15, +1.80]$	$[-1.45, +1.41]$	$[-0.85, +0.79]$
c_{WWWW}/Λ^2	$[-1.32, +1.32]$	$[-2.17, +2.17]$	$[-1.03, +1.03]$	$[-0.79, +0.79]$
$c_{\widetilde{W}}/\Lambda^2$	$[-1.21, +1.21]$	$[-1.96, +1.96]$	$[-4.45, +4.45]$	$[-1.04, +1.04]$

fully hadronic channel dominates the overall $\Delta\chi^2$ with the higher sensitivity in asymmetry in $x - yz$ correlation. In the case of c_{WWWW} , the $4j$ channel maximizes the off-diagonal $A_{W^-W^+}^{x(yz)}$ correlation, capturing CP violation through the relative phases of hadronic W decay amplitudes. The fully leptonic channel maintains $A_{W^-W^+}^{yy}$ sensitivity while minimizing systematic uncertainties from QCD effects (though in reality neutrino reconstruction may

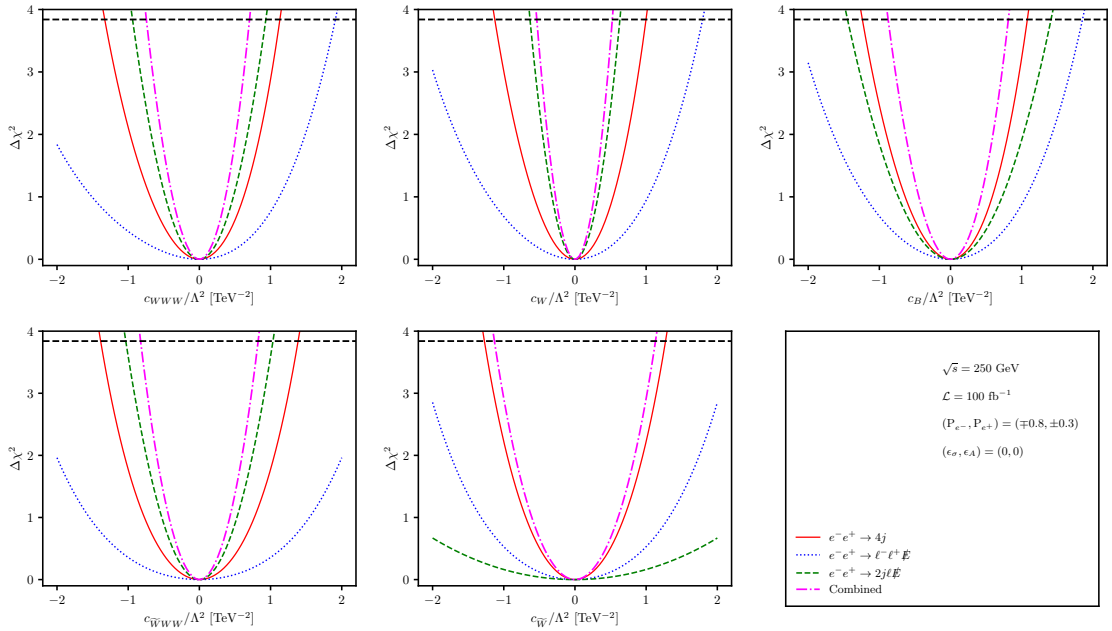


Figure 15: Chi-squared distribution for combination of cross section and asymmetries as a function of one anomalous couplings at a time. The analysis is done for three different decay channel of W^-W^+ di-boson process and their combinations at $\sqrt{s} = 250$ GeV, $\mathcal{L} = 100 \text{ fb}^{-1}$ with two set of beam polarization, $(P_{e^-}, P_{e^+}) = (\mp 0.8, \pm 0.3)$, and zero systematic errors. The horizontal line at $\Delta\chi^2 = 3.84$ represent limit on anomalous couplings at 95% CL. The details of legends and working parameters are given on right most panel of bottom row.

increase the overall theoretical uncertainty). The semileptonic channel exploits $A_{W^-W^+}^{x(yz)}$ correlations providing the most dominant contribution to $\Delta\chi^2$ among three channels. The quadratic rate dependence results in symmetric $\Delta\chi^2$ profiles with minimal discrimination power, emphasizing the critical role of angular observables in probing CP-odd new physics. Thus far, the sensitivity comparison has been performed using unbinned events. For the remainder of the study, the $\Delta\chi^2$ contributions will be aggregated over the eight $\cos\theta^{W^-}$ bins, following the procedure described above.

We present the one-parameter limits on five anomalous WCs obtained from the fully hadronic ($4j$) channel (Fig. 13) and the fully leptonic ($\ell^+\ell^-\not{E}$) channel (Fig. 14) at $\mathcal{L} = 100 \text{ fb}^{-1}$ with beam polarizations $(P_{e^-}, P_{e^+}) = (\mp 0.8, \pm 0.3)$ and zero systematic uncertainties. In each figure, the $\Delta\chi^2$ dependence on a single WC is shown for various observable sets: total cross section (σ), single- W polarization $\mathcal{A}[C_i^{W^\mp}]$, and spin-correlation asymmetries $\mathcal{A}[C_{ij}^{W^-W^+}]$, along with their cumulative combinations. For both channels, σ alone yields the weakest sensitivity, while single- W polarization asymmetries give moderate improvement. The dominant constraints arise from spin-correlation asymmetries, which are highly sensitive to interference among helicity amplitudes. Combining all observables produces the tightest bounds, with the hierarchy of sensitivities and the qualitative $\Delta\chi^2$ shapes being similar between the hadronic and leptonic modes. The horizontal line at $\Delta\chi^2 = 3.84$

corresponds to the 95% CL exclusion for a single degree of freedom.

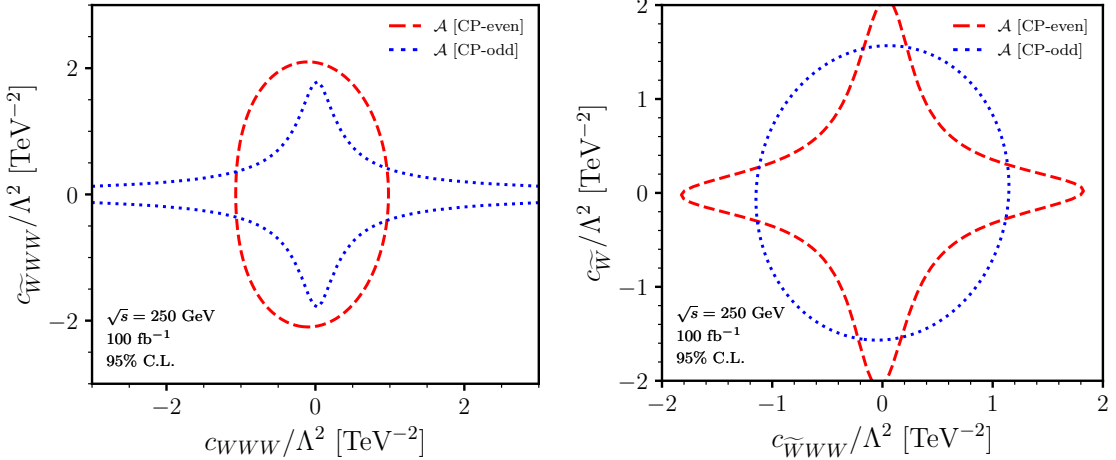


Figure 16: Two-parameter 95% CL contours at $\sqrt{s} = 250$ GeV with 100 fb^{-1} obtained from CP-even (top) and CP-odd (bottom) asymmetries. The CP-even asymmetries dominantly constrain CP-even WCs such as c_{WWW} , while CP-odd asymmetries provide leading, sign-sensitive bounds on CP-odd WCs like $c_{\widetilde{W}WW}$ and $c_{\widetilde{W}}$.

Table 5 presents the 95% CL limits on five dimension-6 WCs obtained from cross sections and asymmetries for three decay channels: $4j$, $\ell^-\ell^+\not{E}$, and $2j\ell\not{E}$ [18], along with combined constraints. The sensitivity varies across operators. For e.g., the CP-even couplings, c_{WWW} and c_W are most tightly constrained by the semileptonic channel, reflecting its balance between event rate and kinematic reconstruction. The WC c_B receives significant contributions from both the semileptonic and fully hadronic channels. The CP-odd operators $c_{\widetilde{W}WW}$ and $c_{\widetilde{W}}$ are best constrained by the fully hadronic channel due to enhanced sensitivity in polarization dependent asymmetries.

Combining all three channels leads to the most stringent limits for all WCs; for instance, the limit on c_{WWW} improves from $[-0.93, +0.93]$ in the semileptonic channel to $[-0.74, +0.70]$ when all channels are combined. All limits are obtained assuming zero systematic uncertainties; the effect of systematics will be discussed later.

Next, we quantify how CP-even and CP-odd observables disentangle the operator structure by performing two-parameter likelihood scans using asymmetries built to be even or odd under CP. Figure 16 (left) shows 95% CL contours in the $(c_{WWW}, c_{\widetilde{W}WW})$ plane derived from a CP-even and CP-odd asymmetry. As expected from CP selection rules, the CP-even asymmetry predominantly constrains the CP-even coefficient c_{WWW} , while being comparatively insensitive to the CP-odd $c_{\widetilde{W}WW}$; conversely, the CP-odd asymmetry dominantly constrains $c_{\widetilde{W}WW}$ and shows weaker dependence on c_{WWW} . The resulting contours are therefore close to orthogonal, and their combination efficiently removes flat directions in the $(c_{WWW}, c_{\widetilde{W}WW})$ plane.

An analogous study in the $(c_{\widetilde{W}WW}, c_{\widetilde{W}})$ plane (Figure 16, right panel) confirms that CP-odd asymmetries provide the leading sensitivity to pairs of CP-odd WCs, while CP-

even asymmetries contribute mainly through quadratic terms and thus exhibit weaker, sign-symmetric contours around the SM point. This complementarity tightens the overall constraints and resolves sign ambiguities that remain in rate-based or CP-even analyses alone.

The utility of asymmetries in this context lies in their ability to disentangle CP structures through interference effects. CP-even (odd) asymmetries pick out the interference of CP-even (odd) operators with the SM, leading to linear and hence sign-sensitive dependence on the corresponding WCs, while suppressing contributions from the opposite CP sector that typically enter only at quadratic order. This results in near-orthogonal constraints from CP-even and CP-odd observables, and their combination collapses otherwise flat directions in the parameter space. Moreover, being ratios of weighted event counts, asymmetries naturally reduce systematic uncertainties associated with luminosity and fiducial kinematic cuts, and by emphasizing kinematic regions where interference is largest, they achieve greater sensitivity than inclusive rate measurements alone.

Having established the complementarity of CP-even and CP-odd observables in disentangling operator structures, we now investigate the robustness of these constraints with respect to experimental inputs. We also consider the case when all five WCs exist simultaneously and the methodology and result for marginalized constraints are discussed in below section.

5.1 MCMC analysis with combined channels

To simultaneously constrain the five WCs, we perform a Markov-Chain-Monte-Carlo (MCMC) analysis based on a global likelihood function constructed from all three decay channels. Each channel is evaluated for both beam polarization configurations, $(P_{e^-}, P_{e^+}) = (\pm 80\%, \mp 30\%)$. The likelihood function is defined as

$$\mathcal{L}(\vec{C}) \propto \exp\left[-\frac{1}{2}\Delta\chi_{\text{tot}}^2(\vec{C})\right], \quad (5.9)$$

where the total chi-squared is expressed as the sum of individual contributions from each final state topology. Each $\Delta\chi^2$ term encapsulates the deviation of the predicted cross sections and weighted asymmetries from the SM expectations, incorporating both statistical and systematic uncertainties. We choose different values of integrated luminosity,

$$\mathcal{L} \in \{100 \text{ fb}^{-1}, 300 \text{ fb}^{-1}, 1000 \text{ fb}^{-1}, 3000 \text{ fb}^{-1}\}, \quad (5.10)$$

where we have used $\mathcal{L}/2$ for each set of beam polarization and systematic errors,

$$(\epsilon_\sigma, \epsilon_A) \in \{(0, 0), (2\%, 1\%), (5\%, 2\%), (10\%, 5\%)\}. \quad (5.11)$$

The covariance structure of the predicted observables is implicitly accounted for through the matrix elements derived from the fitted templates for each polarization configuration. The sampling of the posterior distribution is performed using a random-walk Metropolis algorithm [90, 91] in the five-dimensional parameter space of the WCs, \vec{c} . At each iteration,

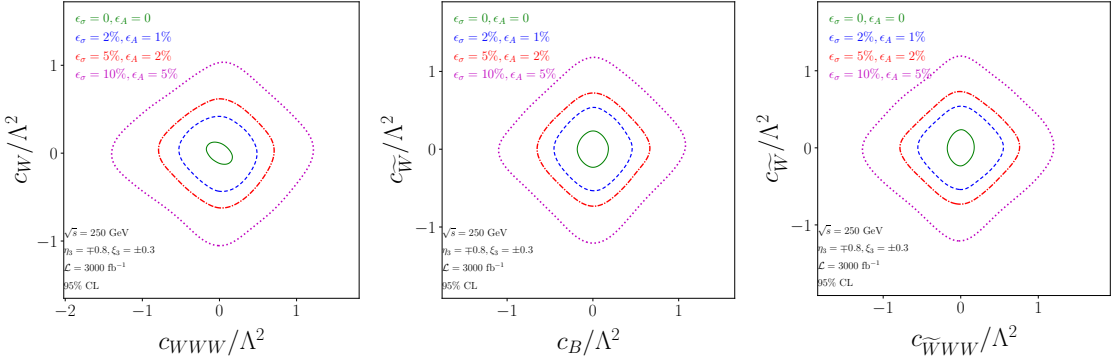


Figure 17: Marginalized 2-D projection at 95% CL from MCMC for a different values of systematic errors. The projections are obtained by combining three decay channels with $\mathcal{L} = 3000 \text{ fb}^{-1}$ for each channel.

a trial point \vec{c}' is generated by applying Gaussian perturbations to the current state \vec{c} , and the move is accepted with probability

$$\rho = \min \left[1, \exp \left(-\frac{1}{2} [\Delta \chi_{\text{tot}}^2(\vec{c}') - \Delta \chi_{\text{tot}}^2(\vec{c})] \right) \right]. \quad (5.12)$$

This procedure efficiently explores the correlated parameter space and yields posterior probability distributions for the WCs that incorporate the combined sensitivity from all decay channels and beam polarizations. The one and two-dimensional densities are computed from the generated MCMC samples using Kernel Density Evaluation implemented in GETDIST [92].

In Fig. 17, we present the 95% CL two-parameter marginalized posterior projections in the (c_{WWWW}, c_W) , $(c_B, c_{\widetilde{W}})$, and $(c_{WWWW}, c_{\widetilde{W}})$ planes for a fixed integrated luminosity of $\mathcal{L} = 3000 \text{ fb}^{-1}$ under varying assumptions on the systematic uncertainties. The contours contract appreciably as the assumed systematic errors are reduced from conservative (10%, 5%) to the idealized case of zero systematics. Quantitatively, the corresponding limits on all five WCs improve by roughly an order of magnitude. For experimentally realistic systematic levels of (2%, 1%), the improvement remains substantial, with the allowed ranges tightening by a factor of approximately three relative to the conservative scenario.

Figure 18 displays the complementary dependence of the 95% CL marginalized contours on the integrated luminosity, for two representative systematic-error configurations, (2%, 1%) and (10%, 5%). In the low-systematic case (top row), the contours exhibit the expected luminosity scaling, shrinking steadily as \mathcal{L} increases. The resulting limits strengthen by factors in the range 1.15–2.20 when \mathcal{L} is increased from 100 to 3000 fb^{-1} . In contrast, for the conservative (10%, 5%) scenario, the contours show only marginal improvement with luminosity, with tightening limited to factors of about 1.10–1.45. This behavior clearly demonstrates that while higher luminosity enhances statistical precision, the ultimate sensitivity is bounded by systematic effects.

To quantitatively summarize these trends, Table 6 reports the one-dimensional marginalized 95% CL intervals for all five WCs across several combinations of integrated luminosity

and systematic uncertainties. These numerical bounds encapsulate the interplay between statistical and systematic contributions to the overall sensitivity. In particular, the steady tightening of the limits with increasing \mathcal{L} at low systematics, and their relative saturation in the high-systematic regime, are clearly reflected in the tabulated results.

Taken together, these studies underscore the complementarity between luminosity-driven statistical gains and systematic-error control. Although increasing \mathcal{L} is vital for short-term sensitivity improvements, systematic uncertainties ultimately dictate the asymptotic precision achievable in global EFT fits. In this context, asymmetry observables—by construction partially canceling correlated systematics—retain a crucial role in extending the reach of higher-dimensional operator searches at future high-luminosity colliders.

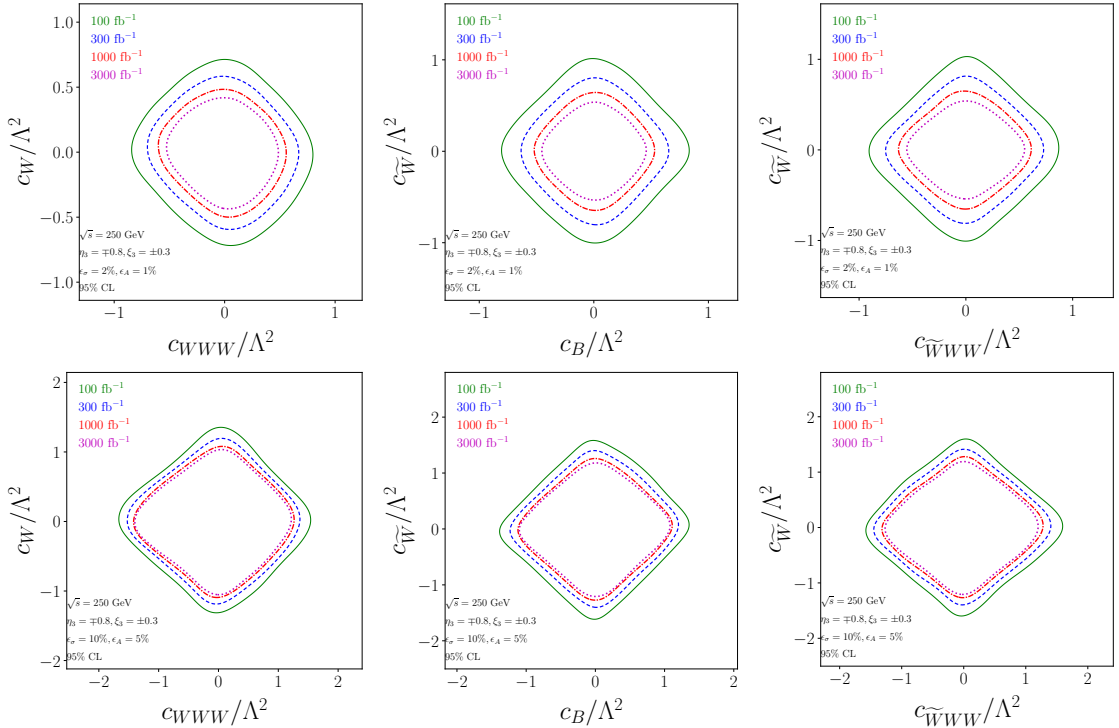


Figure 18: Marginalized 2-D projection at 95% CL from MCMC for a different values of integrated luminosity and systematic error, $(\epsilon_\sigma = 2\%, \epsilon_A = 1\%)$ in top row and $(10\%, 5\%)$ in bottom row. The projections are obtained by combining three decay channels at $\sqrt{s} = 250$ GeV.

6 Conclusion

We have presented a complete leading order study of the process $e^-e^+ \rightarrow W^-W^+$ in three different decay channels at $\sqrt{s} = 250$ GeV within the SMEFT, focusing on deviations in the charged triple gauge couplings. Such deviations arise from dimension-6 operators and manifest as modifications to the W^-W^+V ($V = \gamma, Z$) vertex, which can be systematically probed through polarization and spin correlation observables.

Table 6: Marginalized 95% C.L. limits on the dimension-6 operators obtained with different values of integrated luminosity and systematic error as given in Eq. (5.11).

\mathcal{L} (fb $^{-1}$)	$(\epsilon_\sigma, \epsilon_A)$	c_{WWW}/Λ^2	c_W/Λ^2	c_B/Λ^2	$c_{\widetilde{W}WW}/\Lambda^2$	$c_{\widetilde{W}}/\Lambda^2$
100	(0, 0)	[-1.03, +0.95]	[-0.80, +0.75]	[-1.16, +1.10]	[-1.13, +1.08]	[-1.42, +1.37]
	(2, 1)	[-1.15, +1.13]	[-1.20, +1.15]	[-1.41, +1.35]	[-1.44, +1.52]	[-1.68, +1.75]
	(5, 2)	[-2.06, +1.68]	[-1.72, +1.59]	[-1.87, +1.67]	[-1.78, +1.95]	[-2.17, +2.14]
	(10, 5)	[-3.24, +2.64]	[-2.33, +2.35]	[-2.56, +2.10]	[-2.71, +2.92]	[-2.80, +3.02]
300	(0, 0)	[-0.64, +0.62]	[-0.49, +0.46]	[-0.74, 0.68]	[-0.69, +0.67]	[-0.91, +0.88]
	(2, 1)	[-1.14, +1.02]	[-0.95, +0.88]	[-1.08, +0.97]	[-1.19, +1.20]	[-1.31, +1.30]
	(5, 2)	[-1.80, +1.46]	[-1.45, +1.33]	[-1.49, +1.30]	[-1.57, +1.66]	[-1.66, +1.69]
	(10, 5)	[-2.28, +2.16]	[-2.22, +2.19]	[-2.27, +2.01]	[-2.43, +2.64]	[-2.41, +2.58]
1000	(0, 0)	[-0.38, +0.37]	[-0.28, +0.28]	[-0.42, +0.39]	[-0.40, +0.39]	[-0.52, +0.54]
	(2, 1)	[-0.94, +0.86]	[-0.74, +0.74]	[-0.82, +0.78]	[-1.00, +1.00]	[-1.06, +1.04]
	(5, 2)	[-1.52, +1.18]	[-1.19, +1.16]	[-1.32, +1.17]	[-1.40, +1.48]	[-1.47, +1.41]
	(10, 5)	[-2.22, -1.95]	[-2.01, 1.97]	[-2.25, +1.84]	[-2.28, +2.54]	[-2.24, +2.17]
3000	(0, 0)	[-0.23, +0.23]	[-0.17, +0.17]	[-0.25, +0.24]	[-0.24, +0.23]	[-0.32, +0.32]
	(2, 1)	[-0.79, +0.72]	[-0.65, +0.63]	[-0.72, +0.67]	[-0.85, +0.86]	[-0.81, +0.80]
	(5, 2)	[-1.27, +1.07]	[-1.06, +1.05]	[-1.14, +1.02]	[-1.31, +1.31]	[-1.22, +1.19]
	(10, 5)	[-2.29, +1.94]	[-2.03, +1.98]	[-2.23, +1.97]	[-2.04, +2.33]	[-2.01, +2.00]

We focused on two exclusive final states: the fully hadronic mode ($W^-W^+ \rightarrow 4j$) and the fully leptonic mode ($W^-W^+ \rightarrow \ell^-\nu\ell^+\bar{\nu}$), each of which enables complementary sensitivity to the tensor structure and CP properties of the underlying interactions. For the hadronic channel, we employed a multivariate classification strategy using Boosted Decision Trees (BDTs) to identify and reconstruct the four jets originating from the hadronic decays of the two W bosons. Jet charge variables were used to statistically tag the W^\pm boson charges, while flavor tagging of the final-state jets into up-type or down-type categories was performed via dedicated BDT classifiers, trained on jet substructure and kinematic features.

In the fully leptonic channel, signal discrimination was achieved through optimized cuts on lepton transverse momenta, and di-lepton invariant mass. Given the presence of two missing neutrinos, we utilized a supervised machine learning model—a Multi-Layer Perceptron (MLP)—to regress the complete 4-momenta of the neutrinos, trained on observable quantities such as visible lepton kinematics and missing transverse energy. This enabled full event reconstruction in the dileptonic channel, critical for accessing spin correlation observables.

Having reconstructed the complete event topology in both decay channels, we extracted a set of polarization-sensitive observables and spin correlation asymmetries constructed from the angular distributions of the decay products in the respective boson rest frames. These observables, being linear in the interference between SM and dimension-6 ampli-

tudes, offer enhanced sensitivity to the real and imaginary parts of the Wilson coefficients, including potential CP-violating effects.

Different decay channels are found to be sensitive to different anomalous couplings. For e.g., for the case of \mathcal{O}_B and $\mathcal{O}_{\widetilde{W}}$, we found that $e^-e^+ \rightarrow 4j$ events puts a tighter constrain in comparison to other two decay channels. And for the remaining three operators, the semi-leptonic channel ($2j\ell\cancel{E}$) offer tighter constrain. The Markov-Chain-Monte-Carlo analysis using spin observables along with cross section are performed to set a simultaneous limits on all five WCs at different values of systematic errors and integrated luminosities. We found that in order to put a tighter limits on all WCs, the systematic errors needs to be controlled rather than on increasing the size of datasets.

In summary, this analysis demonstrates the efficacy of combining advanced reconstruction techniques—including machine learning-based kinematic inference—with SMEFT-consistent polarization observables in a clean e^-e^+ collider environment. The complementary treatment of all decay channels of W^-W^+ viz. full-hadronic, semi-leptonic and full-leptonic final states enables a robust and model-independent probe of new physics in the electroweak sector. The framework developed here can be readily extended to higher center-of-mass energies and integrated luminosities, and forms an essential component of the electroweak precision program at future e^-e^+ colliders.

Acknowledgments

Authors thanks R. Rahaman for discussion during the initial phase of this project. A. Subba acknowledges the support of ANRF grant CRG/2023/000580.

References

- [1] UA1 collaboration, *Experimental Observation of Isolated Large Transverse Energy Electrons with Associated Missing Energy at $\sqrt{s} = 540$ GeV*, *Phys. Lett. B* **122** (1983) 103.
- [2] UA2 collaboration, *Observation of Single Isolated Electrons of High Transverse Momentum in Events with Missing Transverse Energy at the CERN anti- p p Collider*, *Phys. Lett. B* **122** (1983) 476.
- [3] UA1 collaboration, *Experimental Observation of Lepton Pairs of Invariant Mass Around 95-GeV/c**2 at the CERN SPS Collider*, *Phys. Lett. B* **126** (1983) 398.
- [4] UA2 collaboration, *Evidence for $Z^0 \rightarrow e^+e^-$ at the CERN $\bar{p}p$ Collider*, *Phys. Lett. B* **129** (1983) 130.
- [5] CMS collaboration, *Measurement of the W^+W^- Cross Section in pp Collisions at $\sqrt{s} = 7$ TeV and Limits on Anomalous $WW\gamma$ and WWZ Couplings*, *Eur. Phys. J. C* **73** (2013) 2610 [[1306.1126](#)].
- [6] CMS collaboration, *Measurement of the $W\gamma$ and $Z\gamma$ Inclusive Cross Sections in pp Collisions at $\sqrt{s} = 7$ TeV and Limits on Anomalous Triple Gauge Boson Couplings*, *Phys. Rev. D* **89** (2014) 092005 [[1308.6832](#)].
- [7] CMS collaboration, *Measurements of the $pp \rightarrow WZ$ inclusive and differential production cross section and constraints on charged anomalous triple gauge couplings at $\sqrt{s} = 13$ TeV*, *JHEP* **04** (2019) 122 [[1901.03428](#)].

[8] CMS collaboration, *Measurement of the inclusive and differential WZ production cross sections, polarization angles, and triple gauge couplings in pp collisions at $\sqrt{s} = 13$ TeV*, *JHEP* **07** (2022) 032 [[2110.11231](#)].

[9] ATLAS collaboration, *Measurement of $W\gamma$ and $Z\gamma$ production cross sections in pp collisions at $\sqrt{s} = 7$ TeV and limits on anomalous triple gauge couplings with the ATLAS detector*, *Phys. Lett. B* **717** (2012) 49 [[1205.2531](#)].

[10] ATLAS collaboration, *Measurement of the WW cross section in $\sqrt{s} = 7$ TeV pp collisions with the ATLAS detector and limits on anomalous gauge couplings*, *Phys. Lett. B* **712** (2012) 289 [[1203.6232](#)].

[11] ATLAS collaboration, *Measurements of $W\gamma$ and $Z\gamma$ production in pp collisions at $\sqrt{s} = 7$ TeV with the ATLAS detector at the LHC*, *Phys. Rev. D* **87** (2013) 112003 [[1302.1283](#)].

[12] ATLAS collaboration, *Measurements of $W^\pm Z$ production cross sections in pp collisions at $\sqrt{s} = 8$ TeV with the ATLAS detector and limits on anomalous gauge boson self-couplings*, *Phys. Rev. D* **93** (2016) 092004 [[1603.02151](#)].

[13] ATLAS collaboration, *Measurements of $Z\gamma$ and $Z\gamma\gamma$ production in pp collisions at $\sqrt{s} = 8$ TeV with the ATLAS detector*, *Phys. Rev. D* **93** (2016) 112002 [[1604.05232](#)].

[14] ATLAS collaboration, *Measurements of $W^+W^- + \geq 1$ jet production cross-sections in pp collisions at $\sqrt{s} = 13$ TeV with the ATLAS detector*, *JHEP* **06** (2021) 003 [[2103.10319](#)].

[15] R. Rahaman and R.K. Singh, *Unravelling the anomalous gauge boson couplings in ZW^\pm production at the LHC and the role of spin-1 polarizations*, *JHEP* **04** (2020) 075 [[1911.03111](#)].

[16] R. Rahaman and R.K. Singh, *Probing the anomalous triple gauge boson couplings in $e^+e^- \rightarrow W^+W^-$ using W polarizations with polarized beams*, *Phys. Rev. D* **101** (2020) 075044 [[1909.05496](#)].

[17] A. Subba and R.K. Singh, *Role of polarizations and spin-spin correlations of W 's in $e^-e^+ \rightarrow W^-W^+$ at $s=250$ GeV to probe anomalous $W-W+Z/\gamma$ couplings*, *Phys. Rev. D* **107** (2023) 073004 [[2212.12973](#)].

[18] A. Subba and R.K. Singh, *Study of anomalous $W^-W^+\gamma/Z$ couplings using polarizations and spin correlations in $e^-e^+ \rightarrow W^-W^+$ with polarized beams*, *Eur. Phys. J. C* **83** (2023) 1119 [[2305.15106](#)].

[19] K. Cheng, Y.-J. Fang, T. Han and M. Low, *Maximizing the Azimuthal-Angle Correlation in the Decay of Vector Boson Pairs*, [2502.14065](#).

[20] M. Diehl and O. Nachtmann, *Optimal observables for the measurement of three gauge boson couplings in $e^+e^- \rightarrow W^+W^-$* , *Z. Phys. C* **62** (1994) 397.

[21] S. Jahedi, J. Lahiri and A. Subba, *Optimal Sensitivity of Anomalous Charged Triple Gauge Couplings through W boson helicity at the e^+e^- colliders*, [2411.13664](#).

[22] S. Chai, J. Gu and L. Li, *From optimal observables to machine learning: an effective-field-theory analysis of $e^+e^- \rightarrow W^+W^-$ at future lepton colliders*, *JHEP* **05** (2024) 292 [[2401.02474](#)].

[23] M. Fabbrichesi, R. Floreanini, E. Gabrielli and L. Marzola, *Stringent bounds on HWW and HZZ anomalous couplings with quantum tomography at the LHC*, *JHEP* **09** (2023) 195 [[2304.02403](#)].

[24] R. Aoude, E. Madge, F. Maltoni and L. Mantani, *Probing new physics through entanglement in diboson production*, *JHEP* **12** (2023) 017 [[2307.09675](#)].

[25] K. Hagiwara, R.D. Peccei, D. Zeppenfeld and K. Hikasa, *Probing the Weak Boson Sector in $e+e- \rightarrow W^+W^-$* , *Nucl. Phys. B* **282** (1987) 253.

[26] C. Degrande, N. Greiner, W. Kilian, O. Mattelaer, H. Mebane, T. Stelzer et al., *Effective Field Theory: A Modern Approach to Anomalous Couplings*, *Annals Phys.* **335** (2013) 21 [[1205.4231](#)].

[27] W. Buchmuller and D. Wyler, *Effective Lagrangian Analysis of New Interactions and Flavor Conservation*, *Nucl. Phys. B* **268** (1986) 621.

[28] B. Grzadkowski, M. Iskrzynski, M. Misiak and J. Rosiek, *Dimension-Six Terms in the Standard Model Lagrangian*, *JHEP* **10** (2010) 085 [[1008.4884](#)].

[29] S. Weinberg, *Baryon and Lepton Nonconserving Processes*, *Phys. Rev. Lett.* **43** (1979) 1566.

[30] K. Hagiwara, S. Ishihara, R. Szalapski and D. Zeppenfeld, *Low-energy effects of new interactions in the electroweak boson sector*, *Phys. Rev. D* **48** (1993) 2182.

[31] G. Buchalla, O. Cata, R. Rahn and M. Schlaffer, *Effective Field Theory Analysis of New Physics in $e+e- \rightarrow W^+W^-$ at a Linear Collider*, *Eur. Phys. J. C* **73** (2013) 2589 [[1302.6481](#)].

[32] D. Choudhury, J. Kalinowski and A. Kulesza, *CP violating anomalous $WW\gamma$ couplings in e^+e^- collisions*, *Phys. Lett. B* **457** (1999) 193 [[hep-ph/9904215](#)].

[33] K. Hagiwara, S. Ishihara, R. Szalapski and D. Zeppenfeld, *Low-energy constraints on electroweak three gauge boson couplings*, *Phys. Lett. B* **283** (1992) 353.

[34] L. Bian, J. Shu and Y. Zhang, *Prospects for Triple Gauge Coupling Measurements at Future Lepton Colliders and the 14 TeV LHC*, *JHEP* **09** (2015) 206 [[1507.02238](#)].

[35] L. Bian, J. Shu and Y. Zhang, *Triple gauge couplings at future hadron and lepton colliders*, *Int. J. Mod. Phys. A* **31** (2016) 1644008 [[1612.03888](#)].

[36] S. Tizchang and S.M. Etesami, *Pinning down the gauge boson couplings in $WW\gamma$ production using forward proton tagging*, *JHEP* **07** (2020) 191 [[2004.12203](#)].

[37] F. Boudjema and R.K. Singh, *A Model independent spin analysis of fundamental particles using azimuthal asymmetries*, *JHEP* **07** (2009) 028 [[0903.4705](#)].

[38] J.A. Aguilar-Saavedra, J. Bernabéu, V.A. Mitsou and A. Segarra, *The Z boson spin observables as messengers of new physics*, *Eur. Phys. J. C* **77** (2017) 234 [[1701.03115](#)].

[39] J.A. Aguilar-Saavedra and J. Bernabeu, *Breaking down the entire W boson spin observables from its decay*, *Phys. Rev. D* **93** (2016) 011301 [[1508.04592](#)].

[40] R. Rahaman and R.K. Singh, *Breaking down the entire spectrum of spin correlations of a pair of particles involving fermions and gauge bosons*, *Nucl. Phys. B* **984** (2022) 115984 [[2109.09345](#)].

[41] A. Alloul, N.D. Christensen, C. Degrande, C. Duhr and B. Fuks, *FeynRules 2.0 - A complete toolbox for tree-level phenomenology*, *Comput. Phys. Commun.* **185** (2014) 2250 [[1310.1921](#)].

[42] N.D. Christensen and C. Duhr, *FeynRules - Feynman rules made easy*, *Comput. Phys. Commun.* **180** (2009) 1614 [[0806.4194](#)].

[43] C. Degrande, C. Duhr, B. Fuks, D. Grellscheid, O. Mattelaer and T. Reiter, *UFO - The Universal FeynRules Output*, *Comput. Phys. Commun.* **183** (2012) 1201 [[1108.2040](#)].

[44] L. Darmé et al., *UFO 2.0: the ‘Universal Feynman Output’ format*, *Eur. Phys. J. C* **83** (2023) 631 [[2304.09883](#)].

[45] J. Alwall, M. Herquet, F. Maltoni, O. Mattelaer and T. Stelzer, *MadGraph 5 : Going Beyond*, *JHEP* **06** (2011) 128 [[1106.0522](#)].

[46] R. Frederix, S. Frixione, V. Hirschi, D. Pagani, H.S. Shao and M. Zaro, *The automation of next-to-leading order electroweak calculations*, *JHEP* **07** (2018) 185 [[1804.10017](#)].

[47] A. Biekötter, B.D. Pecjak, D.J. Scott and T. Smith, *Electroweak input schemes and universal corrections in SMEFT*, *JHEP* **07** (2023) 115 [[2305.03763](#)].

[48] C. Bierlich et al., *A comprehensive guide to the physics and usage of PYTHIA 8.3*, *SciPost Phys. Codeb.* **2022** (2022) 8 [[2203.11601](#)].

[49] DELPHES 3 collaboration, *DELPHES 3, A modular framework for fast simulation of a generic collider experiment*, *JHEP* **02** (2014) 057 [[1307.6346](#)].

[50] C.T. Potter, *DSiD: a Delphes Detector for ILC Physics Studies*, in *International Workshop on Future Linear Colliders*, 2, 2016 [[1602.07748](#)].

[51] R.D. Field and R.P. Feynman, *A Parametrization of the Properties of Quark Jets*, *Nucl. Phys. B* **136** (1978) 1.

[52] Z.-B. Kang, A.J. Larkoski and J. Yang, *Towards a Nonperturbative Formulation of the Jet Charge*, *Phys. Rev. Lett.* **130** (2023) 151901 [[2301.09649](#)].

[53] G. Altarelli and G. Parisi, *Asymptotic Freedom in Parton Language*, *Nucl. Phys. B* **126** (1977) 298.

[54] H.P. Nilles and K.H. Streng, *Quark - Gluon Separation in Three Jet Events*, *Phys. Rev. D* **23** (1981) 1944.

[55] M. Derrick et al., *Comparison of Charged Particle Multiplicities in Quark and Gluon Jets Produced in e^+e^- Annihilation at 29-GeV*, *Phys. Lett. B* **165** (1985) 449.

[56] A. Petersen et al., *Inclusive Charged Particle Distribution in Nearly Threefold Symmetric Three Jet Events at $e(CM) = 29$ -GeV*, *Phys. Rev. Lett.* **55** (1985) 1954.

[57] JADE collaboration, *Experimental Evidence for Differences in p_T Between Quark Jets and Gluon Jets*, *Phys. Lett. B* **123** (1983) 460.

[58] JADE collaboration, *Particle Distribution in Three Jet Events Produced by $e+e-$ Annihilation*, *Z. Phys. C* **21** (1983) 37.

[59] TASSO collaboration, *Comparison of Inclusive Fractional Momentum Distributions of Quark and Gluon Jets Produced in e^+e^- Annihilation*, *Z. Phys. C* **45** (1989) 1.

[60] AMY collaboration, *A comparison of quark and gluon jets produced in high-energy e^+e^- annihilations*, *Phys. Rev. Lett.* **63** (1989) 1772.

[61] S. Marti, J. Chrin, C. Lacasta, J. Valls and J. Fuster, *Differences between quark and gluon jets in DELPHI at LEP*, *Nucl. Phys. B Proc. Suppl.* **39BC** (1995) 131.

[62] OPAL collaboration, *A Study of differences between quark and gluon jets using vertex tagging of quark jets*, *Z. Phys. C* **58** (1993) 387.

[63] OPAL collaboration, *A Direct observation of quark - gluon jet differences at LEP*, *Phys. Lett. B* **265** (1991) 462.

[64] ALEPH collaboration, *Quark and gluon jet properties in symmetric three-jet events*, *Phys. Lett. B* **384** (1996) 353.

[65] ATLAS collaboration, *Light-quark and gluon jet discrimination in pp collisions at $\sqrt{s} = 7$ TeV with the ATLAS detector*, *Eur. Phys. J. C* **74** (2014) 3023 [[1405.6583](#)].

[66] ATLAS collaboration, *Discrimination of Light Quark and Gluon Jets in pp collisions at $\sqrt{s} = 8$ TeV with the ATLAS Detector*, .

[67] ATLAS collaboration, *Quark versus Gluon Jet Tagging Using Charged Particle Multiplicity with the ATLAS Detector*, .

[68] CMS collaboration, *Performance of quark/gluon discrimination in 8 TeV pp data*, .

[69] J. Gallicchio and M.D. Schwartz, *Quark and Gluon Tagging at the LHC*, *Phys. Rev. Lett.* **107** (2011) 172001 [[1106.3076](#)].

[70] CMS collaboration, *Study of quark and gluon jet substructure in Z+jet and dijet events from pp collisions*, *JHEP* **01** (2022) 188 [[2109.03340](#)].

[71] CMS collaboration, *Measurements of jet charge with dijet events in pp collisions at $\sqrt{s} = 8$ TeV*, *JHEP* **10** (2017) 131 [[1706.05868](#)].

[72] ATLAS collaboration, *Quark versus Gluon Jet Tagging Using Jet Images with the ATLAS Detector*, .

[73] P.T. Komiske, E.M. Metodiev and M.D. Schwartz, *Deep learning in color: towards automated quark/gluon jet discrimination*, *JHEP* **01** (2017) 110 [[1612.01551](#)].

[74] C. Szegedy, W. Liu, Y. Jia, P. Sermanet, S. Reed, D. Anguelov et al., *Going deeper with convolutions*, 9, 2014, DOI [[1409.4842](#)].

[75] J. Barnard, E.N. Dawe, M.J. Dolan and N. Rajcic, *Parton Shower Uncertainties in Jet Substructure Analyses with Deep Neural Networks*, *Phys. Rev. D* **95** (2017) 014018 [[1609.00607](#)].

[76] L.G. Almeida, M. Backović, M. Cliche, S.J. Lee and M. Perelstein, *Playing Tag with ANN: Boosted Top Identification with Pattern Recognition*, *JHEP* **07** (2015) 086 [[1501.05968](#)].

[77] L. de Oliveira, M. Kagan, L. Mackey, B. Nachman and A. Schwartzman, *Jet-images — deep learning edition*, *JHEP* **07** (2016) 069 [[1511.05190](#)].

[78] J. Cogan, M. Kagan, E. Strauss and A. Schwartzman, *Jet-Images: Computer Vision Inspired Techniques for Jet Tagging*, *JHEP* **02** (2015) 118 [[1407.5675](#)].

[79] M. Andrews, J. Alison, S. An, P. Bryant, B. Burkle, S. Gleyzer et al., *End-to-end jet classification of quarks and gluons with the CMS Open Data*, *Nucl. Instrum. Meth. A* **977** (2020) 164304 [[1902.08276](#)].

[80] J.S.H. Lee, I. Park, I.J. Watson and S. Yang, *Quark-Gluon Jet Discrimination Using Convolutional Neural Networks*, *J. Korean Phys. Soc.* **74** (2019) 219 [[2012.02531](#)].

[81] H. Qu and L. Gouskos, *ParticleNet: Jet Tagging via Particle Clouds*, *Phys. Rev. D* **101** (2020) 056019 [[1902.08570](#)].

[82] M. He and D. Wang, *Quark/gluon discrimination and top tagging with dual attention transformer*, *Eur. Phys. J. C* **83** (2023) 1116 [[2307.04723](#)].

[83] P.T. Komiske, E.M. Metodiev and J. Thaler, *Energy Flow Networks: Deep Sets for Particle Jets*, *JHEP* **01** (2019) 121 [[1810.05165](#)].

[84] ATLAS collaboration, *Performance and calibration of quark/gluon-jet taggers using 140 fb^{-1} of pp collisions at TeV with the ATLAS detector**, *Chin. Phys. C* **48** (2024) 023001 [[2308.00716](#)].

[85] E. Alvarez, M. Spannowsky and M. Szewc, *Unsupervised Quark/Gluon Jet Tagging With Poissonian Mixture Models*, *Front. Artif. Intell.* **5** (2022) 852970 [[2112.11352](#)].

[86] M.J. Dolan, J. Gargalionis and A. Ore, *Quark-versus-gluon tagging in CMS Open Data with CWoLa and TopicFlow*, [2312.03434](#).

[87] CMS collaboration, *Quark-gluon Jet Discrimination At CMS*, in *2nd Large Hadron Collider Physics Conference*, 9, 2014 [[1409.3072](#)].

[88] E. Bols, J. Kieseler, M. Verzetti, M. Stoye and A. Stakia, *Jet Flavour Classification Using DeepJet*, *JINST* **15** (2020) P12012 [[2008.10519](#)].

[89] ATLAS collaboration, *Performance of missing transverse momentum reconstruction with the ATLAS detector using proton-proton collisions at $\sqrt{s} = 13$ TeV*, *Eur. Phys. J. C* **78** (2018) 903 [[1802.08168](#)].

[90] N. Metropolis, A.W. Rosenbluth, M.N. Rosenbluth, A.H. Teller and E. Teller, *Equation of state calculations by fast computing machines*, *J. Chem. Phys.* **21** (1953) 1087.

[91] W.K. Hastings, *Monte Carlo Sampling Methods Using Markov Chains and Their Applications*, *Biometrika* **57** (1970) 97.

[92] A. Lewis, *GetDist: a Python package for analysing Monte Carlo samples*, *JCAP* **08** (2025) 025 [[1910.13970](#)].